Appendix I. Microphone Properties

The pressure microphones used both inside and outside the trumpet were 1/10″ diameter Knowles Acoustics FG-23329 high-performance omni-directional microphones. This microphone's sensitivity is -53dB ±3dB up to 10 kHz as shown in Figure 38.[10]
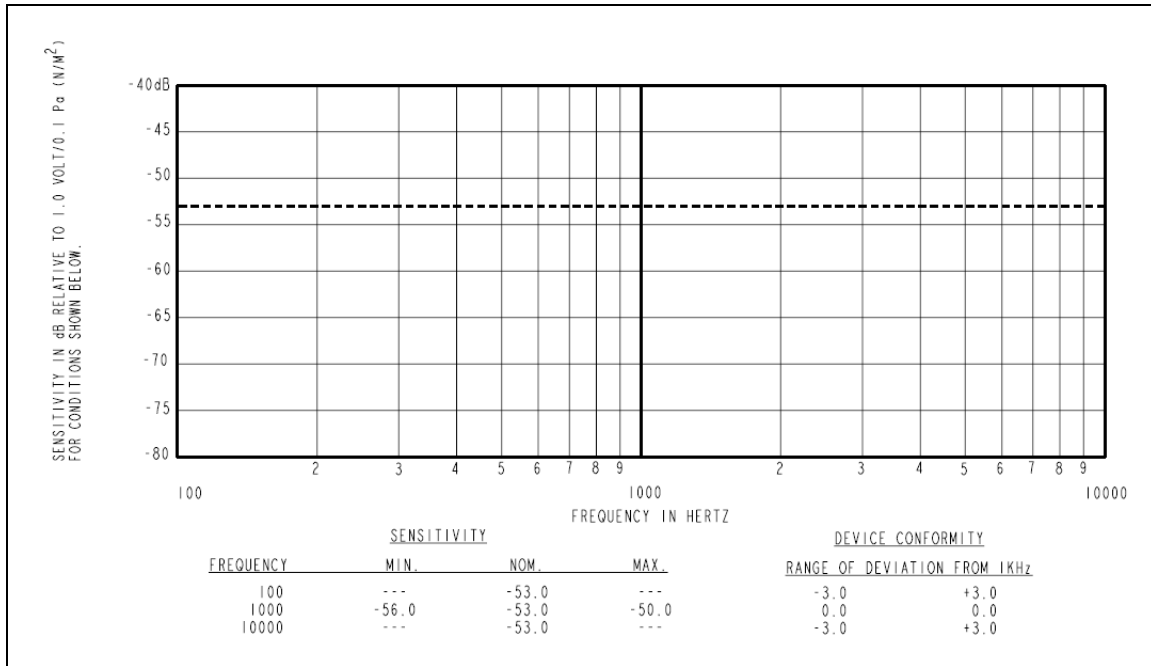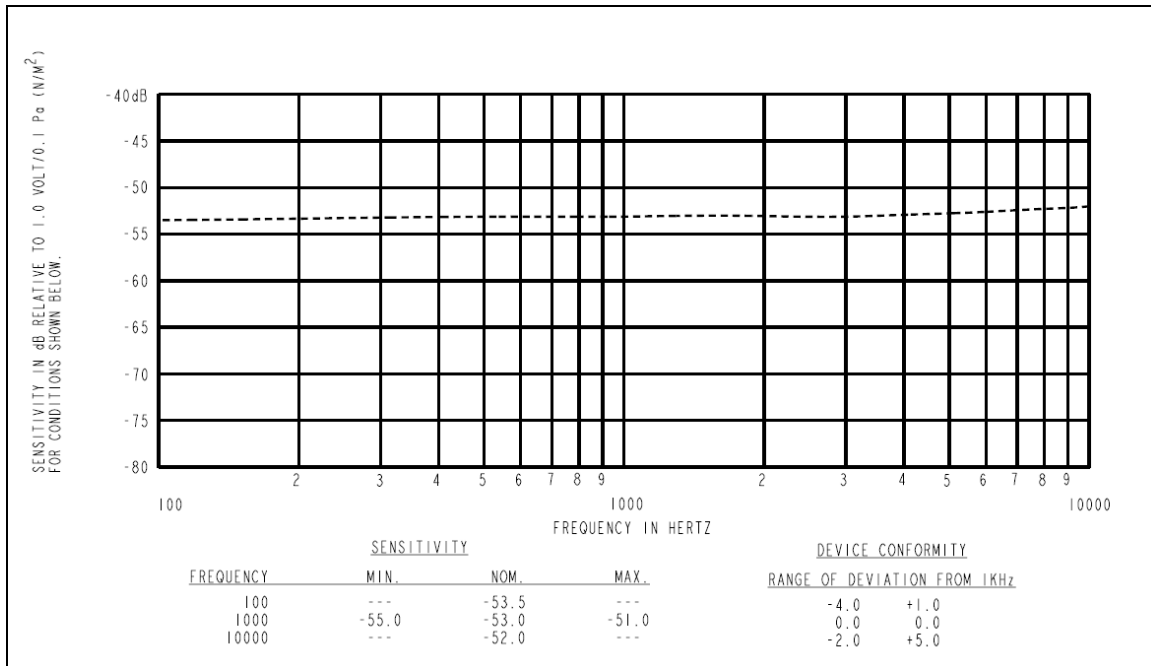

Figure 38. Sensitivity of the Knowles Acoustics FG-23329 high-performance omni-directional microphone up to a frequency of 10 kHz. Note: This plot is taken directly from the Knowles Acoustics FG-23329 technical datasheet.[10]

The microphone used to measure internal particle velocity was a modified Knowles Acoustics EK-23132 high-performance omni-directional microphone. This microphone's sensitivity is -53dB ±2dB up to 10 kHz as shown in Figure 39.[11]

SENSITIVITY IN dB RELATIVE TO 1.0 VOLT/0.1 Pa (N/M²) FOR CONDITIONS SHOWN BELOW.

-40dB
-45
-50
-55
-60
-65
-70
-75
-80

FREQUENCY IN HERTZ

100   1000   10000

	SENSITIVITY			DEVICE CONFORMITY	
FREQUENCY	MIN.	NOM.	MAX.	RANGE OF DEVIATION FROM 1KHz	
100	- - -	-53.5	- - -	-4.0	+1.0
1000	-55.0	-53.0	-51.0	0.0	0.0
10000	- - -	-52.0	- - -	-2.0	+5.0

Figure 39. Sensitivity of the Knowles Acoustics EK-23132 high-performance omni-directional microphone up to a frequency of 10 kHz. Note: This plot is taken directly from the Knowles Acoustics EK-23132 technical datasheet.[11]

The microphone used to measure the external particle velocity was a modified 0.38" diameter RadioShack 270-090 omni-directional microphone. This microphone has a sensitivity of -64dB ±2dB and a flat frequency response over the range of interest for the trumpet.[12]

The Knowles Acoustics/RadioShack pressure and particle velocity microphone noise spectra is shown in Figure 40. The sudden rise in noise as the frequency decreases is due to *1/f* noise due to the ventilation system in the room where the noise spectra were obtained.
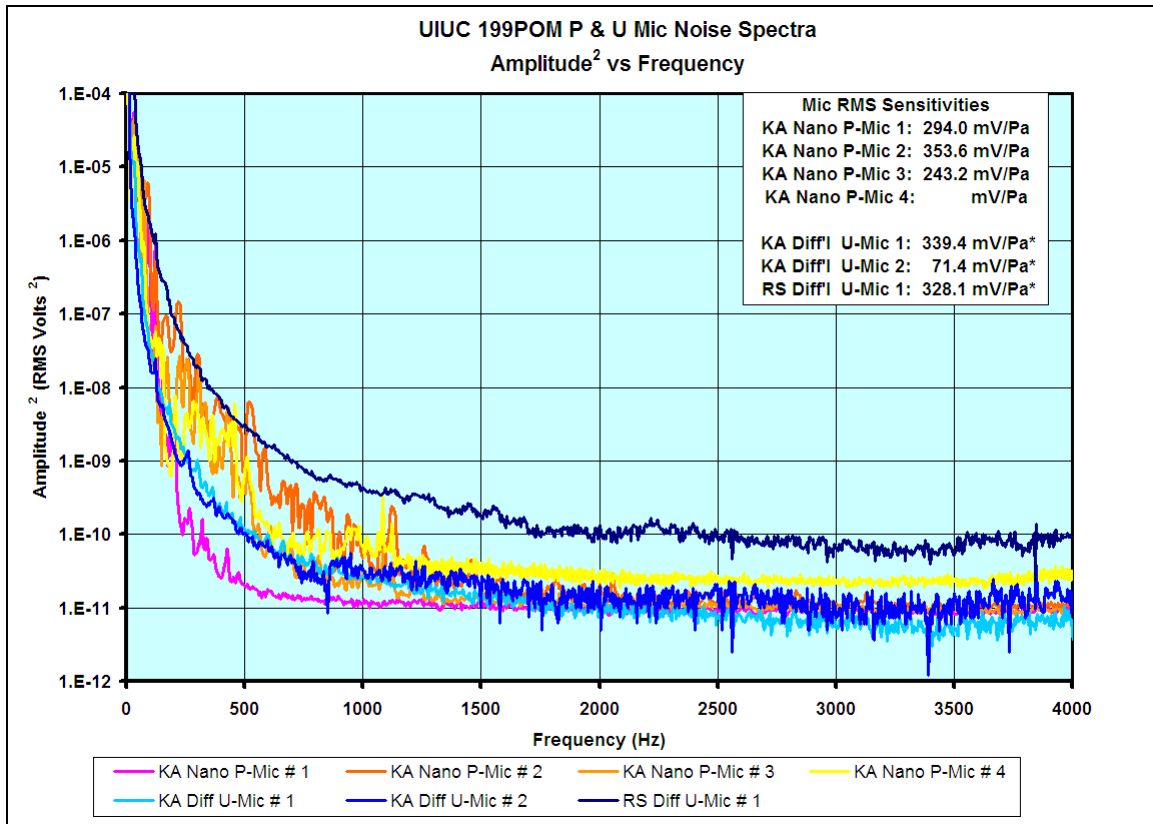
Figure 40. Knowles Acoustics/RadioShack pressure and particle velocity noise spectra up to 4000 Hz.

Appendix II. Microphone/Preamp Electronics Phase Corrections

The experimental setup used to measure the particle velocity and pressure induced in a driven Bb trumpet has inherent phase shifts associated with the various equipment used to take the measurements. Thus corrections to these phase shifts must be applied to the complex raw pressure and particle velocity data in order to obtain the true real and imaginary components of these quantities. The phase corrections were obtained using a custom built standing wave tube (SWT)—arguably the simplest musical instrument— driven with an identical piezo transducer as used with the trumpet. The SWT was constructed from a stainless steel vacuum tube and is 1.209 m in length and 6.0 cm in

diameter. An identical custom built KA particle-velocity microphone and a KA pressure microphone as used with the trumpet measurements was inserted into the far end of the SWT opposite the piezo transducer. A RS particle-velocity microphone and a KA pressure microphone were placed outside the tube in proximity to the piezo transducer. The measurement techniques were identical to those of the trumpet. A picture of our SWT experimental setup is shown in Figure 41.

Figure 41. Picture of the setup of the SWT used for calibration. SWT was driven by a piezoelectric driver on the right end of the tube. Internal pressure and particle velocity measurements were taken by microphones located at the left end of the tube.

When plotted, the raw real and imaginary components of both the complex pressure and particle velocity show a frequency-dependent combination of real and

imaginary parts. A frequency dependent phase correction angle, $\varphi_c(f)$ degrees, was

therefore obtained from the raw phase data in order to rotate the real and imaginary

components of our measurements in the complex plane, thereby making the real particle

velocity and pressure purely real and the imaginary particle velocity and pressure purely
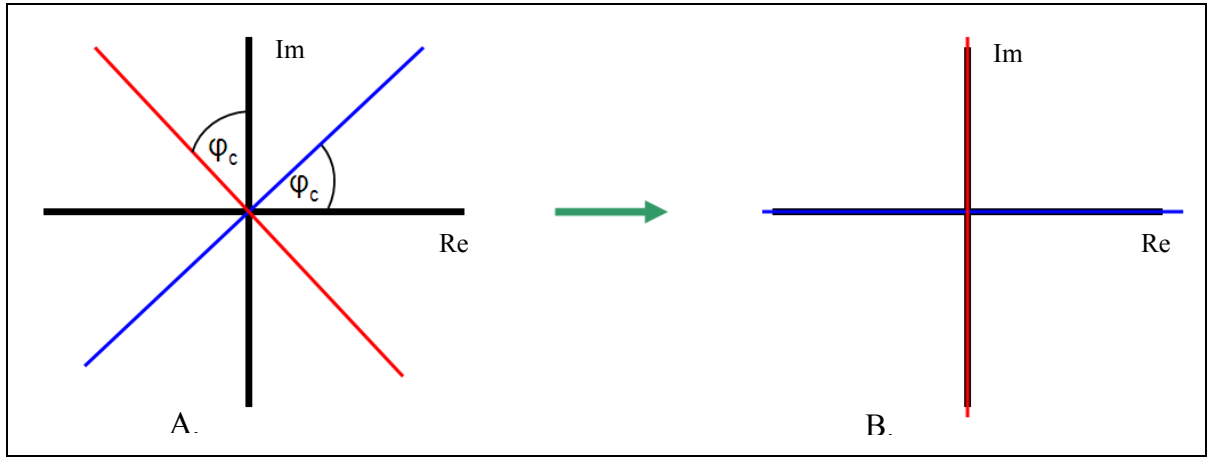
imaginary (Figure 42).

Figure 42. A. Real (blue) and imaginary (red) components of either pressure or particle velocity in the complex plane under the influence of a phase shift, φ_c. B. After phase correction is applied the real and imaginary components are shifted by φ_c thereby making the real component purely real and the imaginary component purely imaginary.

This phase correction was obtained using a rotation matrix in the complex plane

where X_{obs} and Y_{obs} are the measured values of the real and imaginary components,

respectively, and X_{corr} and Y_{corr} are the phase corrected real and imaginary components,

respectively (Equations 1a-1b).

$$\begin{pmatrix} X_{obs}(f) \\ Y_{obs}(f) \end{pmatrix} = \begin{pmatrix} Cos\left[\varphi_c(f)\right] & Sin\left[\varphi_c(f)\right] \\ -Sin\left[\varphi_c(f)\right] & Cos\left[\varphi_c(f)\right] \end{pmatrix} \begin{pmatrix} X_{corr}(f) \\ Y_{corr}(f) \end{pmatrix} \quad \text{(1a)}$$

$$\begin{pmatrix} X_{corr}(f) \\ Y_{corr}(f) \end{pmatrix} = \begin{pmatrix} Cos[\varphi_c(f)] & -Sin[\varphi_c(f)] \\ Sin[\varphi_c(f)] & Cos[\varphi_c(f)] \end{pmatrix} \begin{pmatrix} X_{obs}(f) \\ Y_{obs}(f) \end{pmatrix} \quad \text{(1b)}$$

This rotation matrix provides the formulas needed to convert measured values of the real and imaginary components of pressure and particle velocity to phase corrected values (Equations 2a-2c).

$$X_{corr}(f) = X_{obs}(f) * Cos[\varphi_c(f)] - Y_{obs}(f) * Sin[\varphi_c(f)] \quad \text{(2a)}$$

$$Y_{corr}(f) = X_{obs}(f) * Sin[\varphi_c(f)] + Y_{obs}(f) * Cos[\varphi_c(f)] \quad \text{(2b)}$$

$$\text{and: } \varphi_{corr}(f) = \arctan\left(\frac{Y_{corr}(f)}{X_{corr}(f)}\right) \quad \text{(2c)}$$

The raw real and imaginary internal/external pressure as a function of frequency are shown in Figure 43 and Figure 44, respectively. To find the frequency dependent $\varphi_c(f)$ for the internal KA pressure microphone and the external KA pressure microphone, the raw phase plot was examined (Figure 45). For the internal KA pressure microphone, the points at which the phase was changing the least were determined. These points occurred halfway between the zero crossings of the internal phase plot. These points were then plotted as a function of frequency and a sixth degree polynomial fit was used to fit the curve (Figure 46). This sixth degree polynomial fit—with the +90° ignored—determines how the internal pressure $\varphi_c(f)$ changes with frequency (Equation 3).
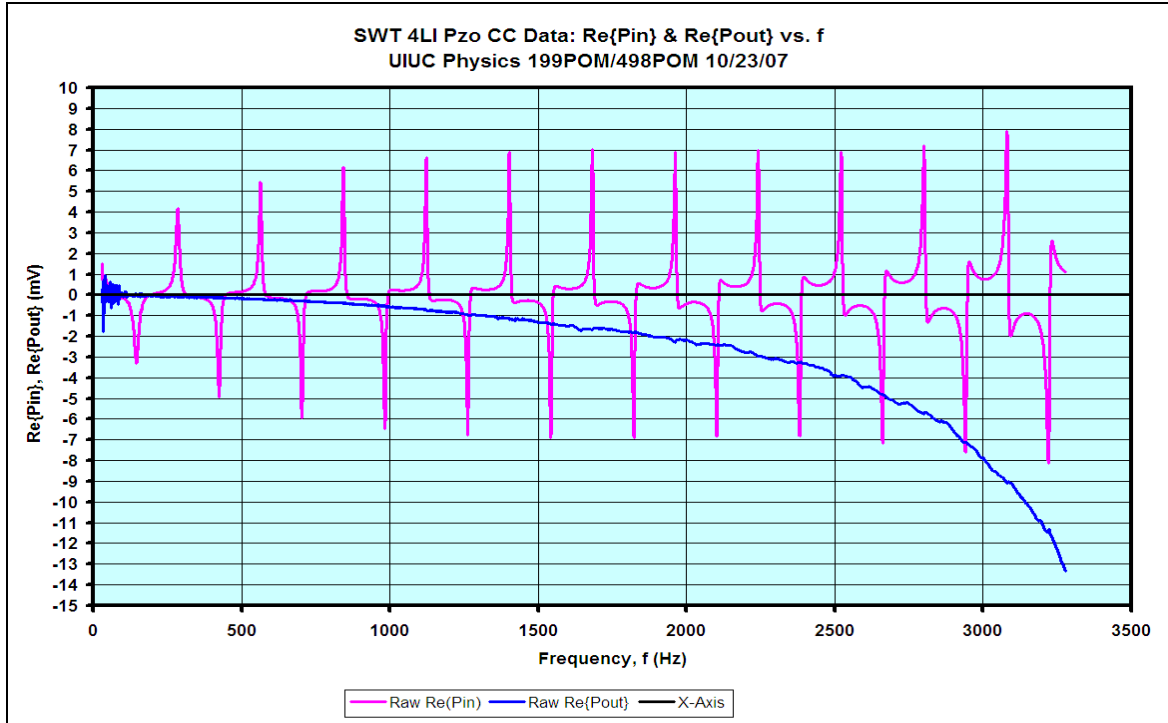
Figure 43. Raw real component of the internal (pink) and external (blue) pressure of the SWT as a function of frequency. Real internal pressure starts real, but, as frequency increases, becomes more imaginary.
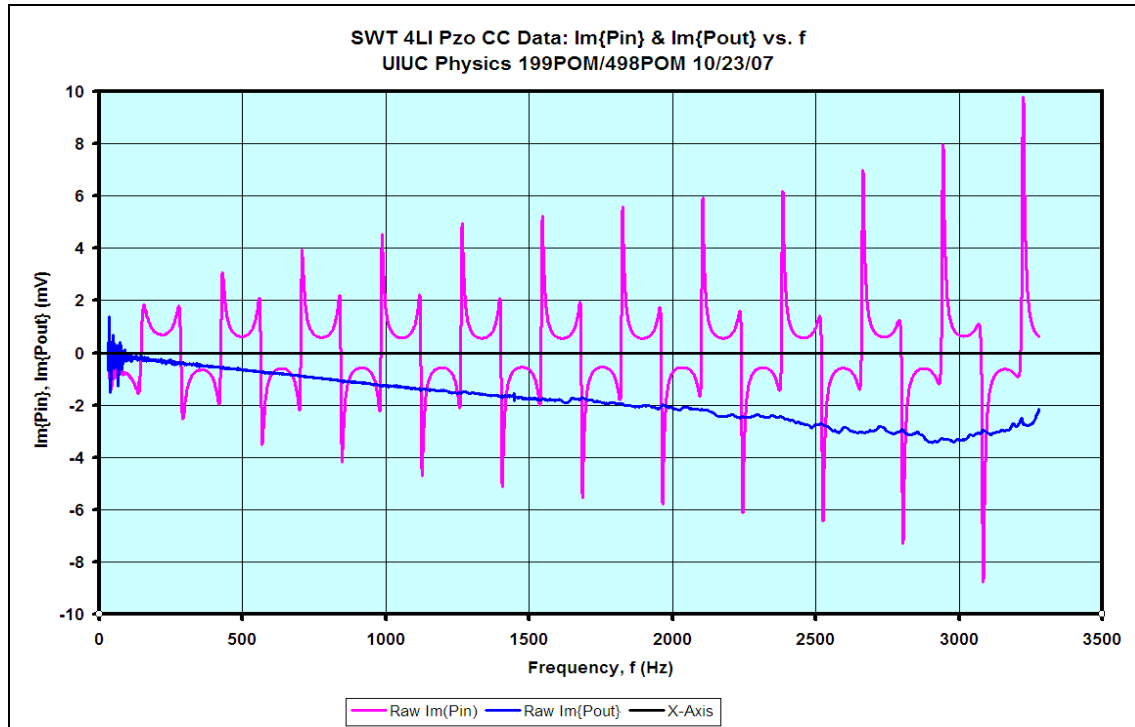

Figure 44. Raw imaginary component of the internal (pink) and external (blue) pressure as a function of frequency. The imaginary internal pressure starts imaginary, but, as frequency increase, becomes more real.
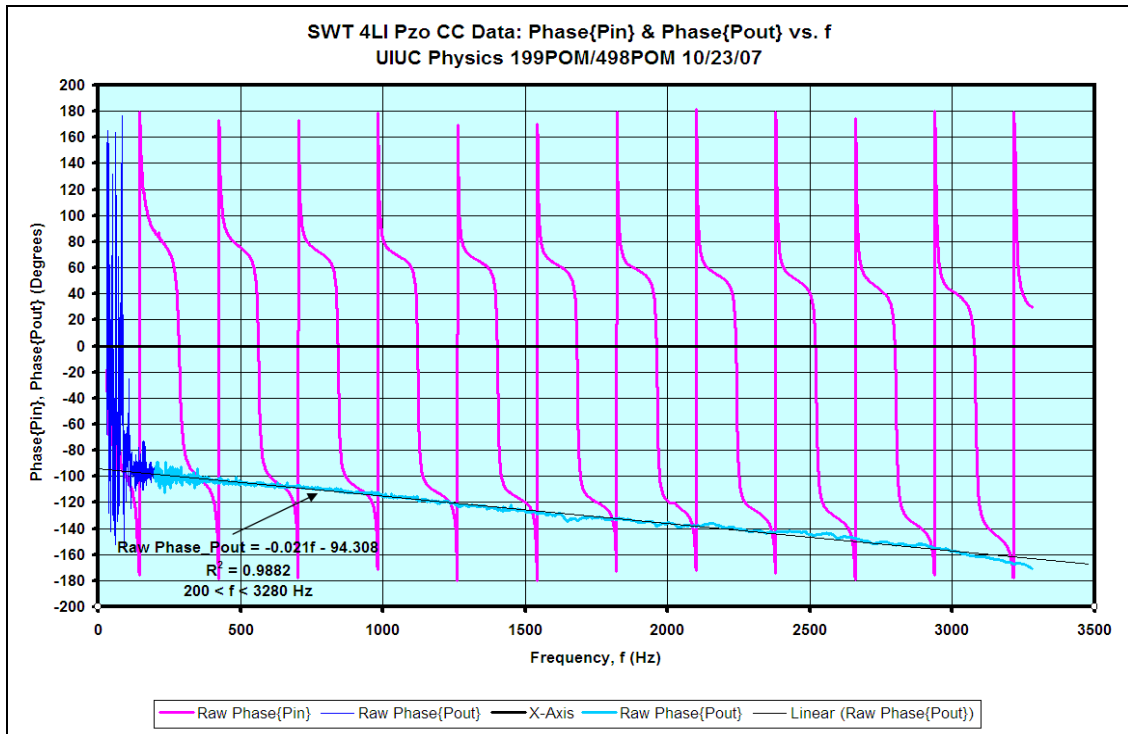
Figure 45. Raw phase plot of both the internal (pink) and the external (blue) pressure as a function of frequency.
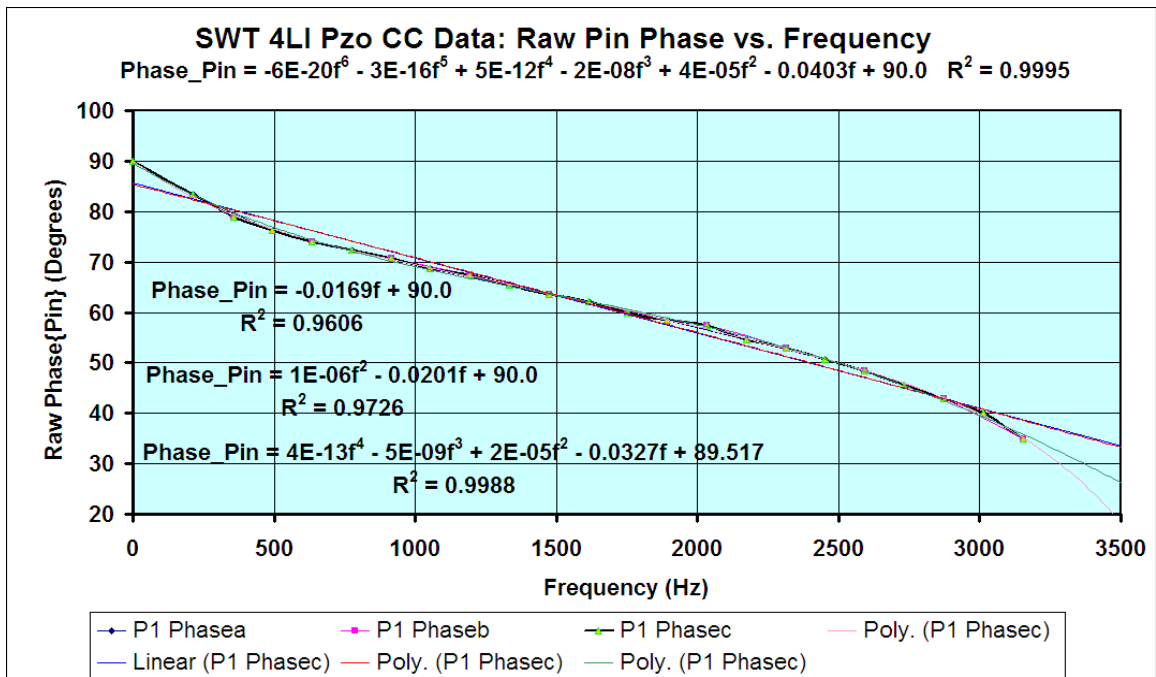
Figure 46. Various polynomial fits to a plot of the frequency values at which the phase change of the internal KA pressure microphone is least severe (midpoints between zero crossings). Sixth degree polynomial was used to determine $\varphi_c(f)$ for the internal pressure microphone.

$$\varphi_{c_{P_{in}}} = -(4.109\text{E-}2*f) + (3.68799\text{E-}5*f\char`\^2) - (2.18667\text{E-}8*f\char`\^3) \ldots$$
$$+ (5.95431\text{E-}12*f\char`\^4) - (5.11865\text{E-}16*f\char`\^5) - (3.62788\text{E-}20*f\char`\^6) \tag{3}$$

Determining the $\varphi_c(f)$ for external KA pressure microphone was more straightforward. Since the phase changed linearly with frequency, a linear fit of the external pressure phase was used and a slope of -0.021 was found. The slope of the linear fit reveals how the external pressure $\varphi_c(f)$ changes with frequency (Equation 4).

$$\varphi_{c_{P_{out}}} = -0.021*f \tag{4}$$

Using the values of $\varphi_c(f)$ for either the internal pressure or external pressure coupled with Equations 2a-c, the corrected Re(P), Im(P), and φ_p can be plotted as functions of frequency (Figures 47, 48, and 49 respectively).
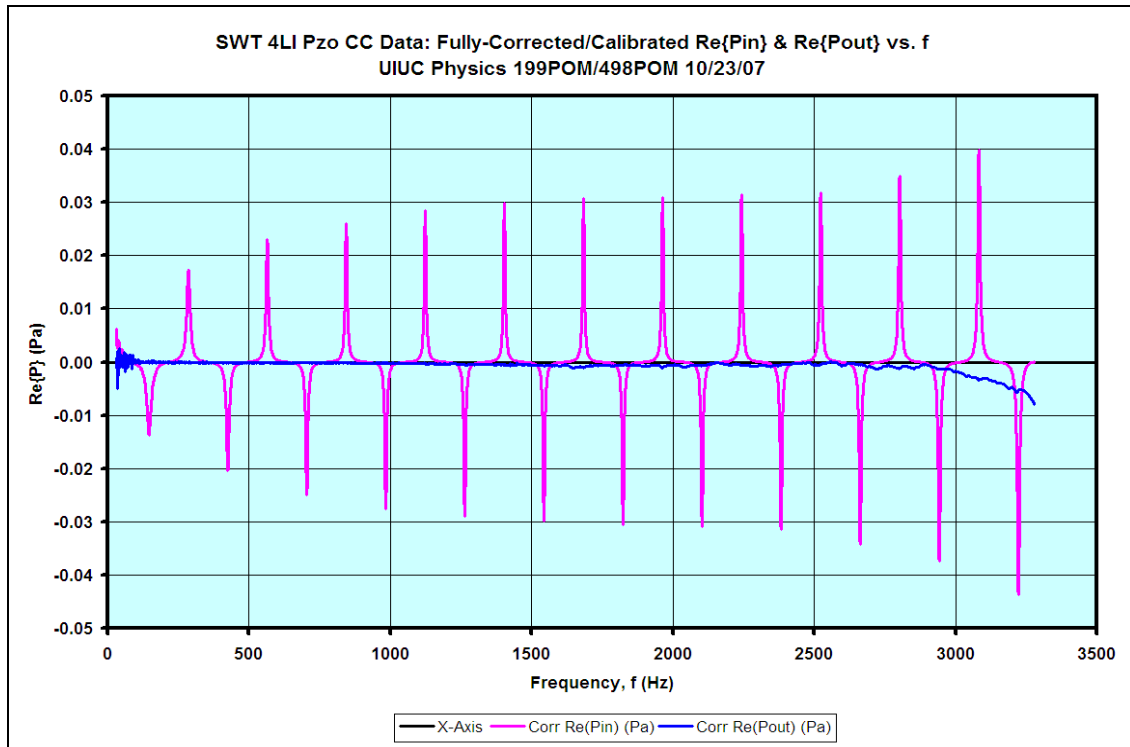
Figure 47. Phase corrected real component of internal (pink) and external (blue) pressure as a function of frequency. The real component of the internal pressure remains real up to ~3000 Hz and beyond.
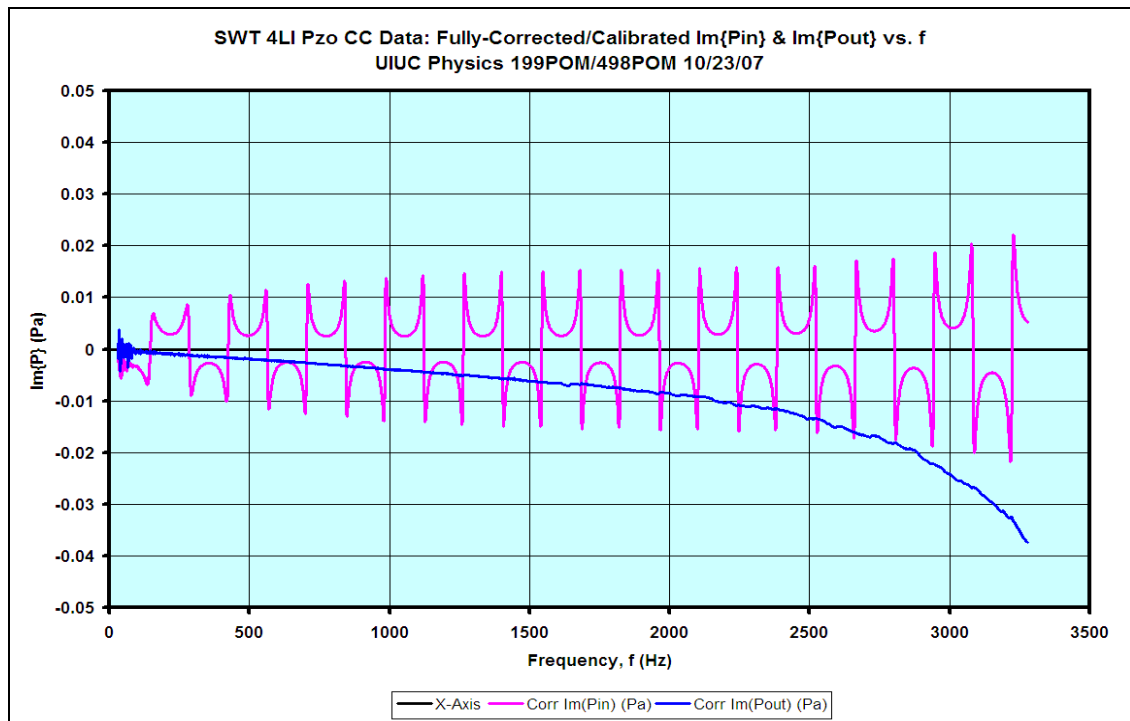
Figure 48. Phase corrected imaginary component of internal (pink) and external (blue) pressure as a function of frequency. The imaginary internal pressure remains imaginary up to ~3000 Hz and beyond.
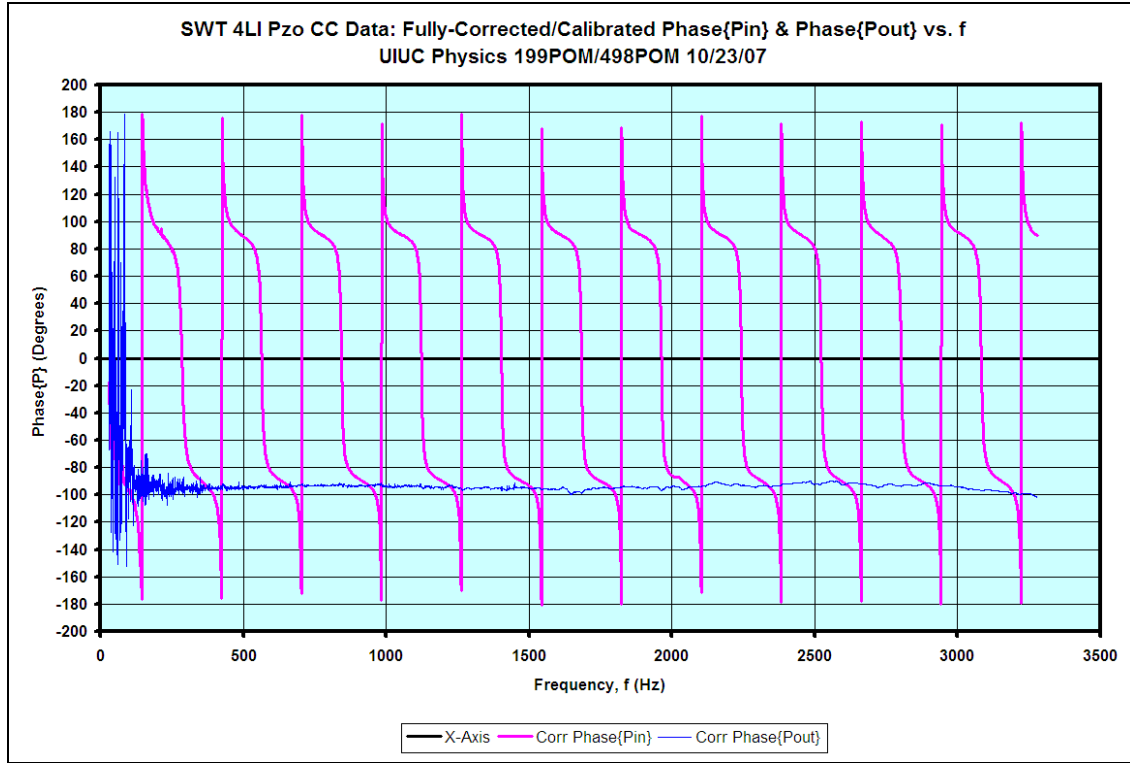
Figure 49. Corrected phase plots as a function of frequency for both the internal (pink) and external (blue) KA pressure microphones.

The raw real and imaginary internal/external particle velocity as a function of frequency are shown in Figure 50 and Figure 51, respectively. Since the particle velocity is 90° out of phase for the SWT data, "imaginary looking" plots are expected for the real component of the particle velocity and "real looking" plots are expected for the imaginary component of the pressure. A similar process to obtain $\varphi_c(f)$ for the KA pressure microphones was used to find $\varphi_c(f)$ for both the RS and KA particle velocity microphones. The $\varphi_c(f)$'s for both the internal KA particle velocity microphone and external RS particle velocity microphone were found by examining the raw phase plot for each microphone (Figure 52).

The points at which the phase of the internal KA particle-velocity microphone changes least rapidly were found and plotted. A sixth order polynomial fit was mapped

onto the curve (Figure 53). This polynomial fit—keeping the ~90° term at the end—

shows the frequency dependence of $\varphi_c(f)$ for the internal KA particle velocity microphone

(Equation 5).
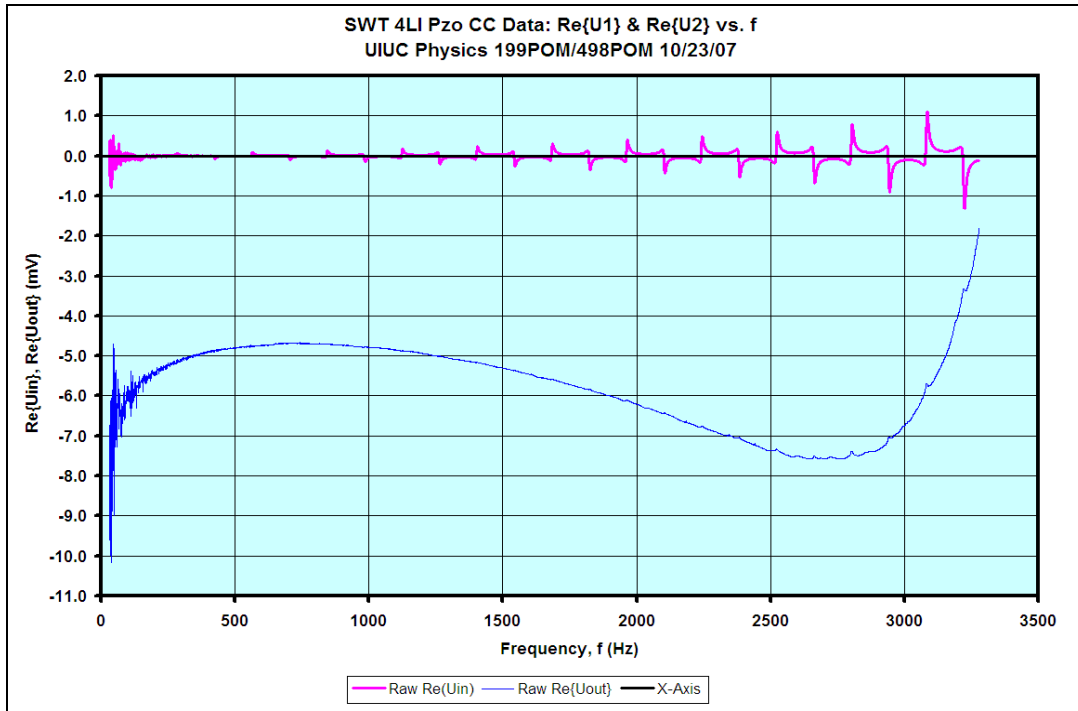
Figure 50. Raw real component of the internal (pink) and external (blue) particle velocity of the SWT as a function of frequency. Real component of the internal particle velocity starts real, but, as frequency increases, becomes more imaginary.
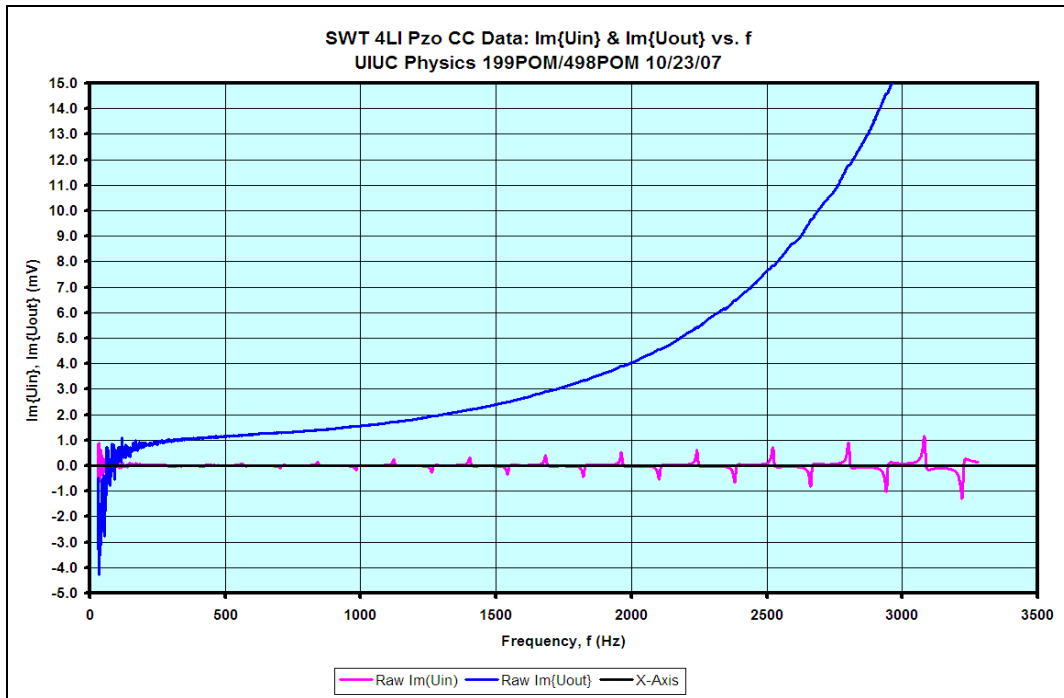
Figure 51. Raw imaginary component of the internal (pink) and external (blue) particle velocity as a function of frequency. The imaginary internal pressure starts real, but, as frequency increase, becomes more imaginary.
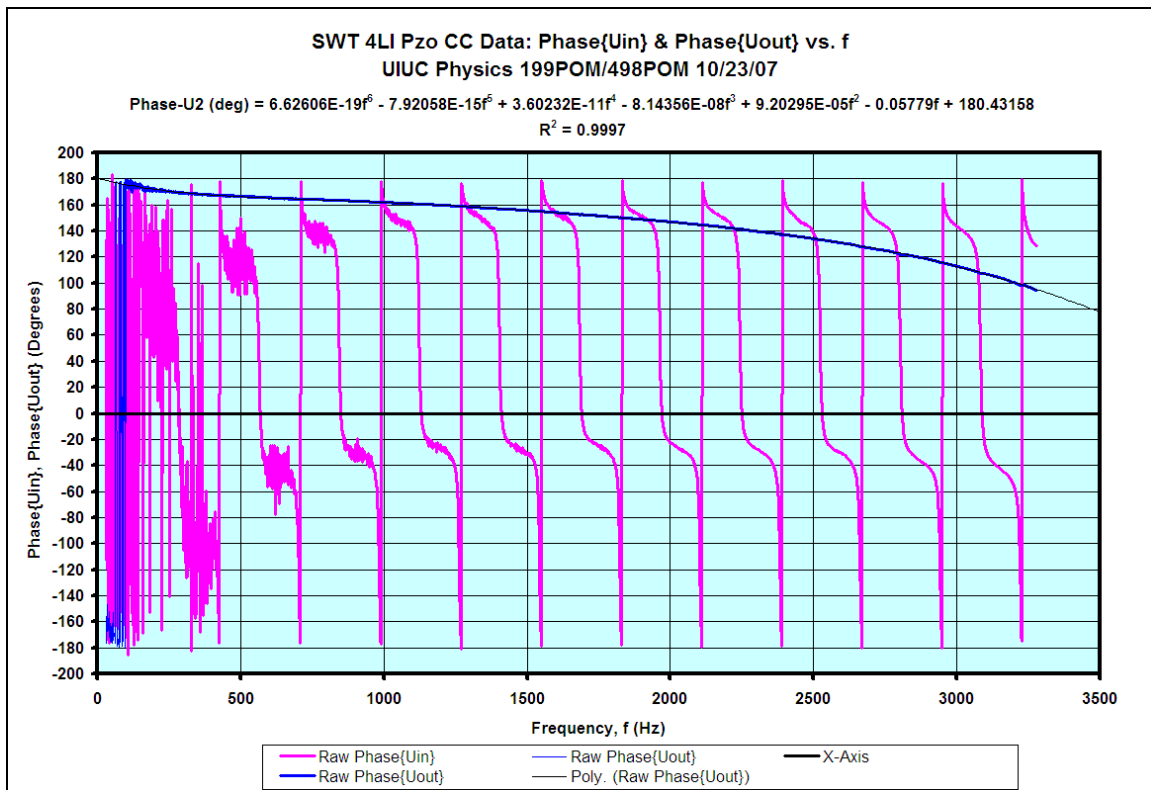
Figure 52. Raw phase plot of both the internal (pink) and the external (blue) particle velocity as a function of frequency.
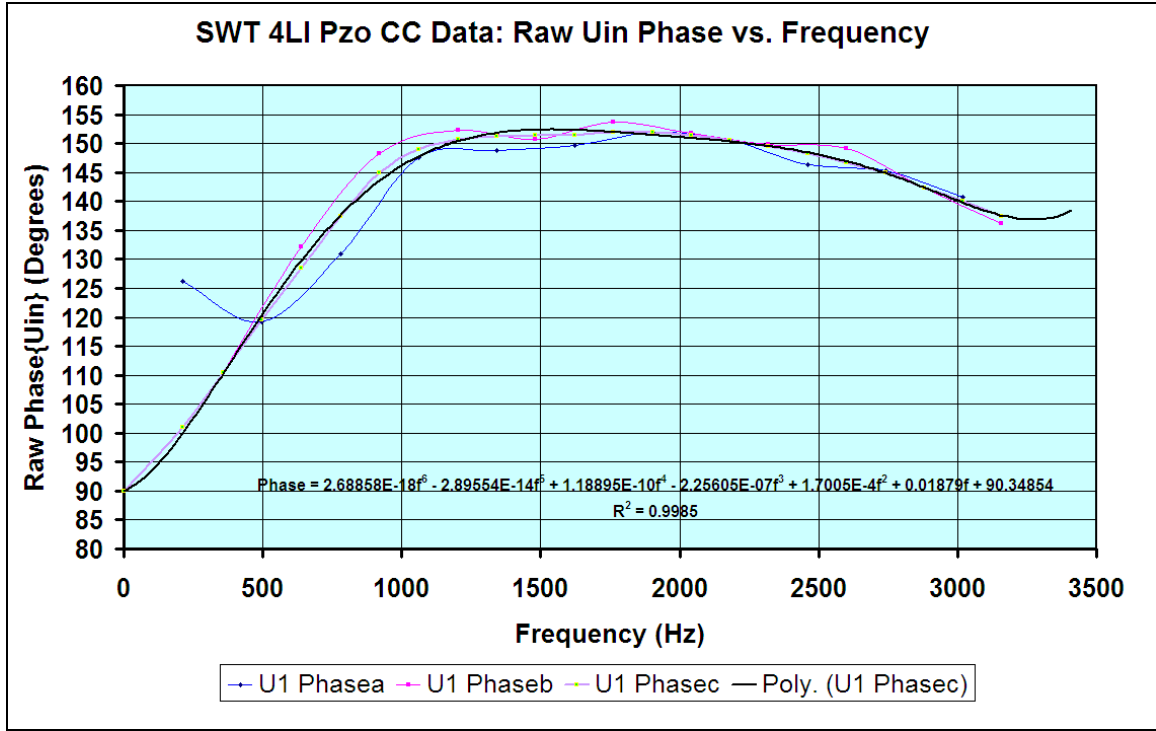
Figure 53. Plots of the frequency values at which the phase change of the internal KA particle-velocity microphone is least severe (midpoints between zero crossings). Sixth degree polynomial was used to determine φc(f) for the internal KA particle-velocity microphone.

$$\varphi_{C_{U_{in}}} = (2.68858E\text{-}18*f\char`^6) - (2.89554E\text{-}14*f\char`^5) + (1.18895E\text{-}10*f\char`^4) \ldots$$
$$- (2.25605E\text{-}07*f\char`^3) + (1.7005E\text{-}4*f\char`^2) + (0.01879*f) + 90° \tag{5}$$

The full raw phase as a function of frequency for the external particle velocity microphone was fit with a sixth order polynomial to obtain the φc(f) for the external RS particle velocity microphone (Equation 6).

$$\varphi_{C_{U_{out}}} = (6.62606E\text{-}19*f\char`^6) - (7.92058E\text{-}15*f\char`^5) + (3.60232E\text{-}11*f\char`^4)\ldots$$
$$- (8.14356E\text{-}08*f\char`^3) + (9.20295E\text{-}05*f\char`^2) - (0.05779*f) + 90° \tag{6}$$

Using the values of $\varphi_c(f)$ for either the internal particle velocity or external

particle velocity coupled with Equations 2a-c, the corrected Re(U), Im(U), and φ_u can be

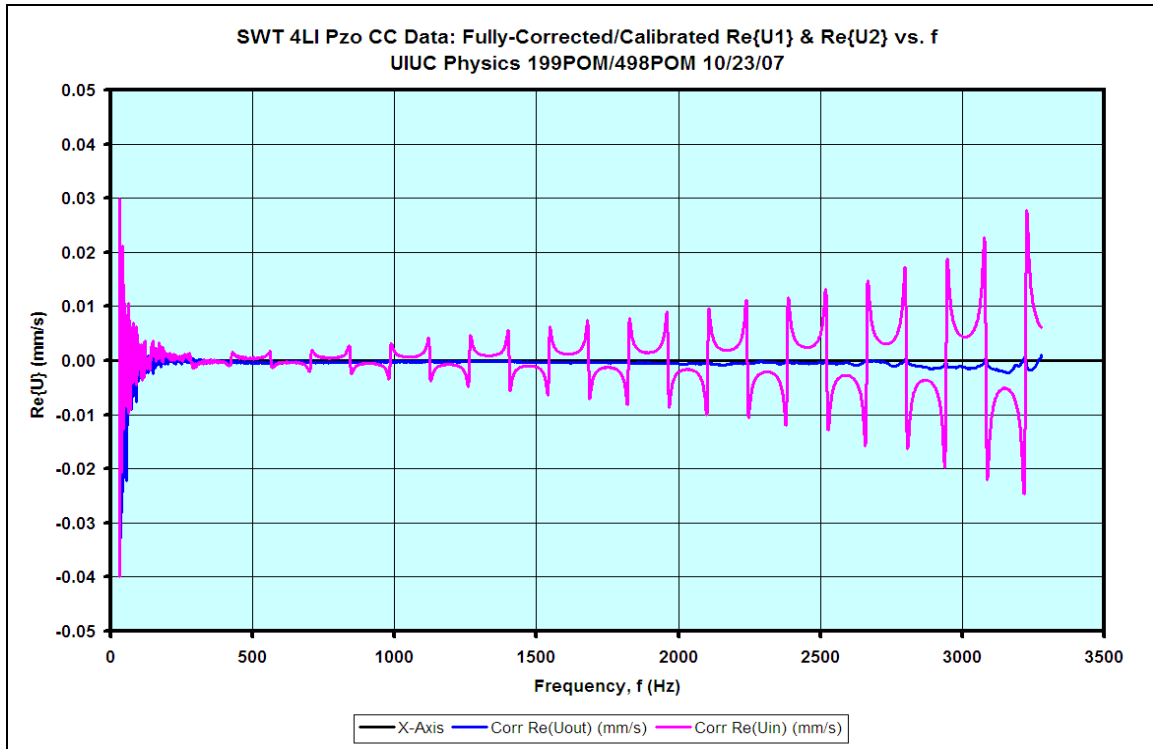plotted as functions of frequency (Figures 54, 55, and 56 respectively).

Figure 54. Phase corrected real component of internal (pink) and external (blue) particle velocity as a function of frequency. The real component of the internal particle velocity remains real up to ~3000 Hz and beyond.
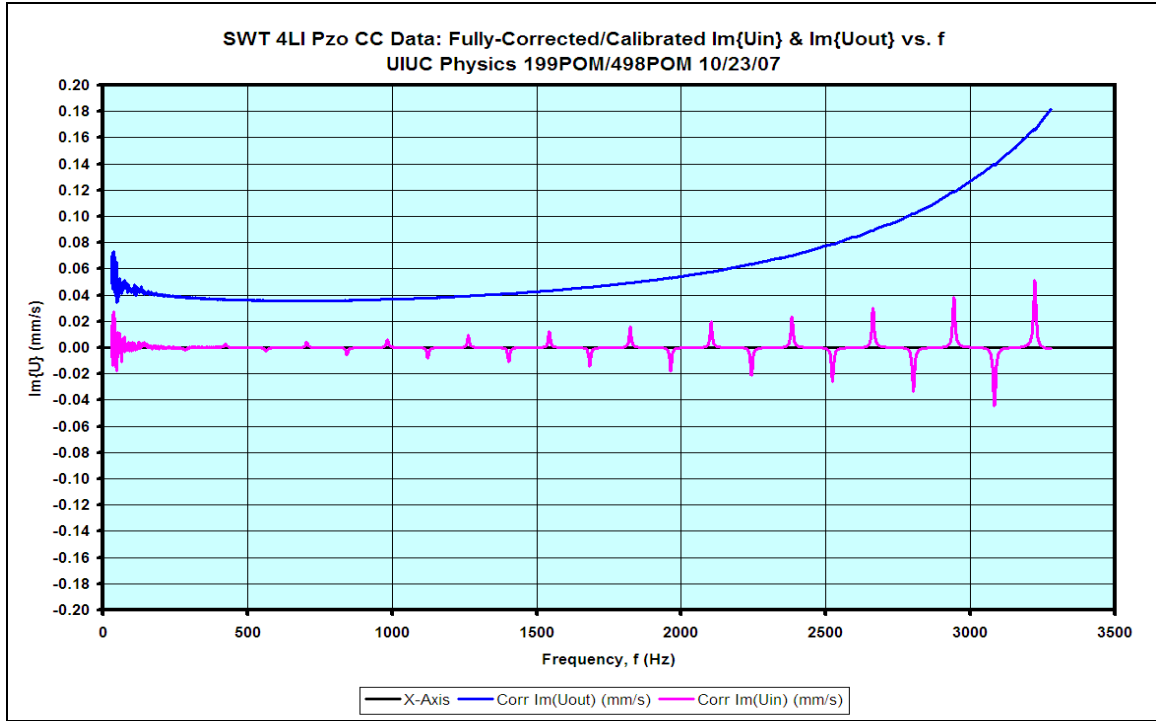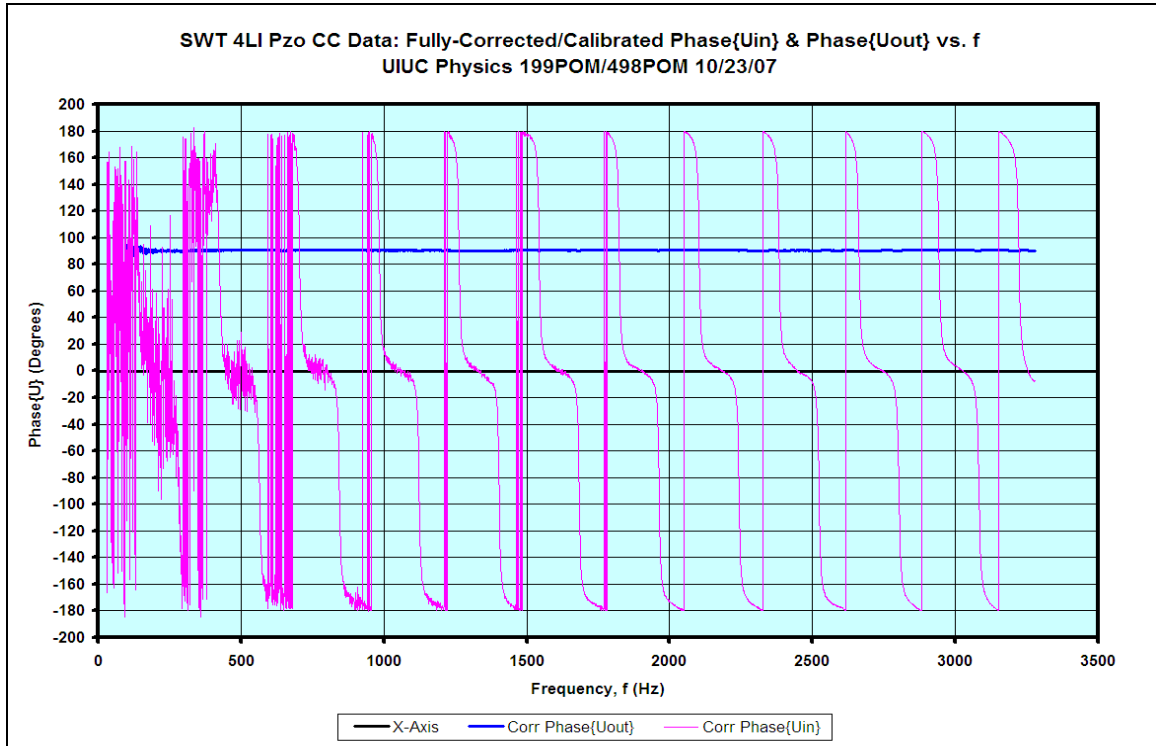
Figure 55. Phase corrected imaginary component of internal (pink) and external (blue) particle velocity as a function of frequency. The imaginary internal particle velocity remains imaginary up to ~3000 Hz and beyond.

Figure 56. Corrected phase plots as a function of frequency for both the internal KA particle velocity microphone (pink) and external RS particle velocity microphone (blue).

The microphones and preamps used for the trumpet analysis are extremely similar to the microphones used for the SWT. Thus, the same phase corrections used for the SWT can be directly applied to the trumpet.

Appendix III. SWT Results and Phase Confirmation

Once the phase corrections have been applied to the SWT data, the impedance and intensity results obtained provides additional insight on the validity of our phase corrections.

The real component of the internal/external impedance as a function of frequency is shown in Figure 57. The imaginary component of the internal/external impedance as a function of frequency is shown in Figure 58. These results confirm the validity of our phase corrections for the external microphones. Since pressure and particle velocity are in phase with each other for 1-D plane waves in a free sound field, the external impedance outside of the SWT in proximity to the piezo-transducer must be an entirely real quantity.[13] Figure 57 confirms that the external impedance of the SWT has a predominantly real component and Figure 58 confirms that the external impedance has little to no imaginary component. Thus, the magnitude of the external impedance—shown in Figure 59—is nearly entirely real as predicted.

The internal impedance of the SWT is quite noisy with a few extremely narrow peaks. This lack of a clearly defined hierarchy of internal impedance peaks explains why a large, closed, stainless steel tube is a musically uninteresting instrument.
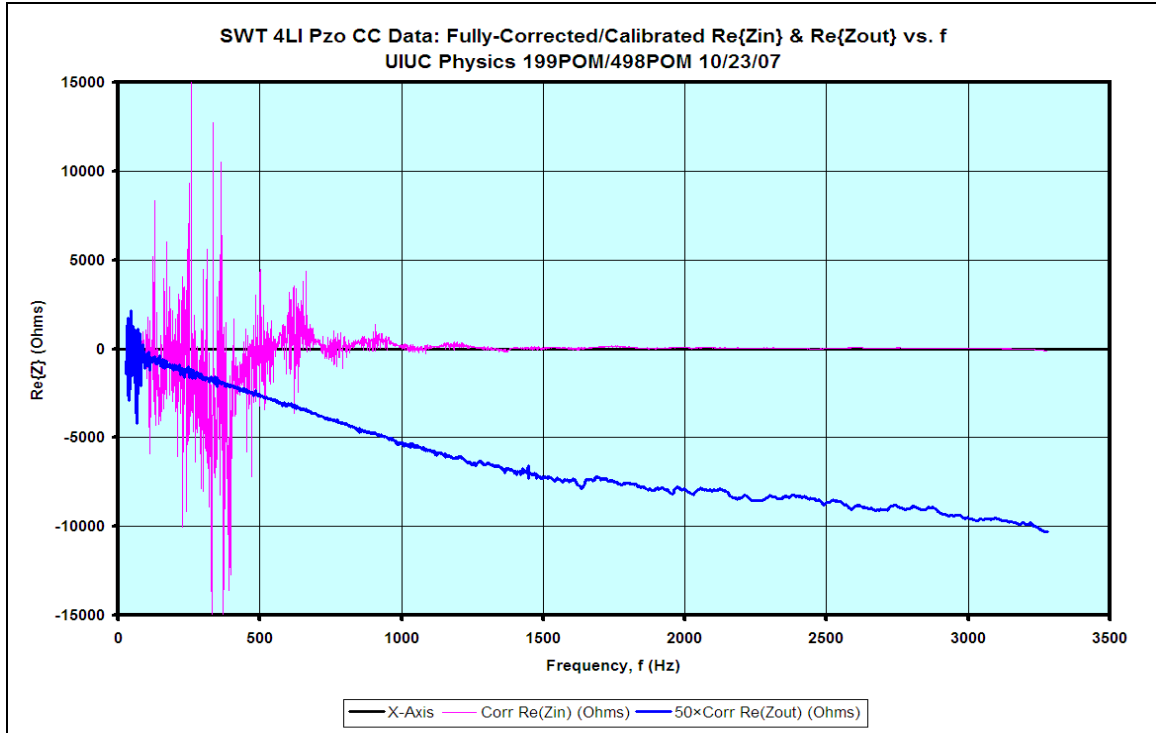
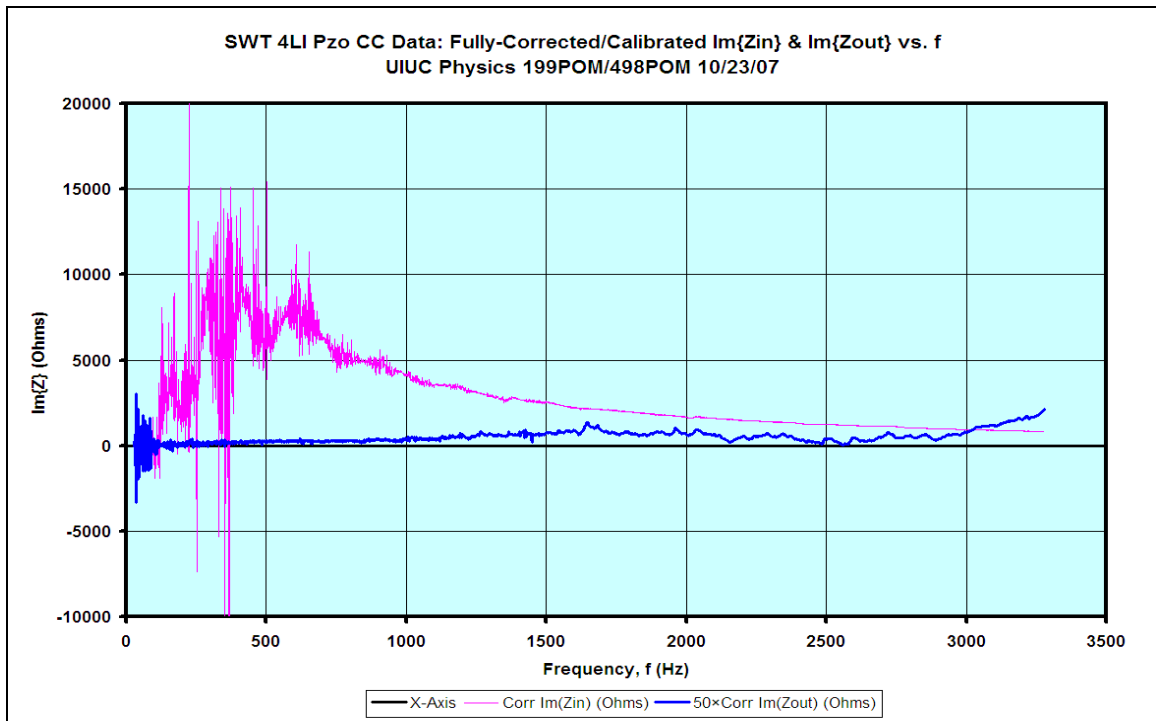*Figure 57. Real component of the internal (pink) and 50×external (blue) impedance as a function of frequency.*

Figure 58. Imaginary component of the internal (pink) and 50×external (blue) impedance as a function of frequency. The imaginary component of the external impedance is essentially zero as predicted by 1-D plane waves propagating in a free sound field.
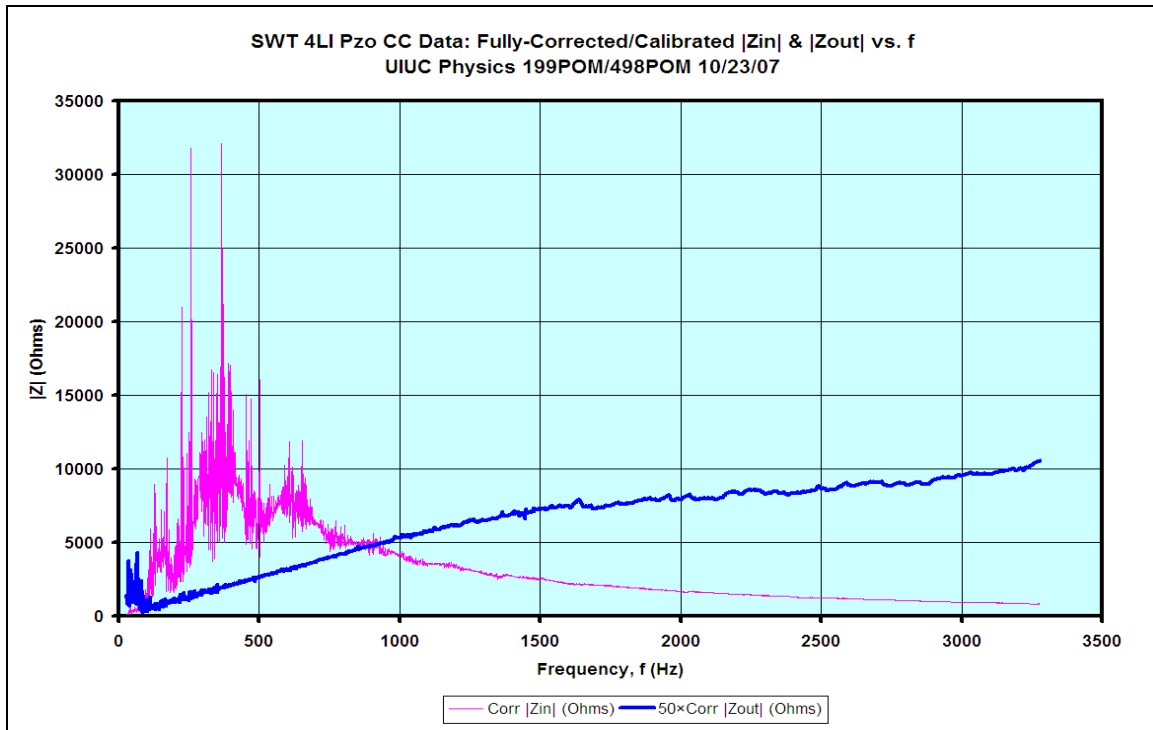
Figure 59. Magnitude of the internal (pink) and 50×external (blue) impedance as a function of frequency.

Since the phase correction of the external microphones has correctly been determined, confirmation of the validity of the phase correction of the internal microphones is needed. A standing wave inside a tube closed on both ends is comprised of two equal-amplitude, counter-propagating, traveling plane waves. Since only a propagating traveling plane wave can have a non-zero real component of longitudinal intensity, a standing wave's longitudinal intensity must be purely imaginary.[13] Thus, the real and imaginary components of the complex longitudinal intensity can be used to confirm the phase corrections for the internal microphones. Figure 60 shows the real component of the internal longitudinal intensity is on the order of a few nW/m^2. Figure 61 shows the imaginary component of the longitudinal intensity—which is on the order of hundreds of nW/m^2—is what makes up the vast majority of the magnitude of

the longitudinal complex intensity (Figure 62). The phase corrected data for internal

microphones agree with predicted results of internal longitudinal complex intensity

thereby explicitly verifying the performed phase corrections.

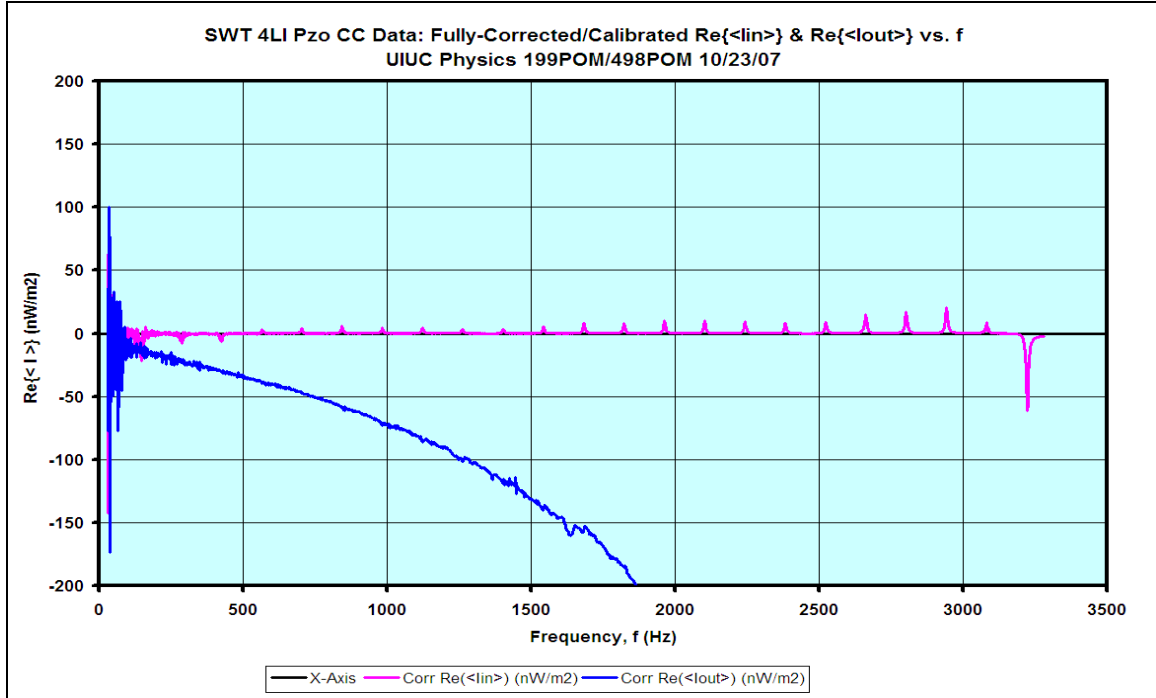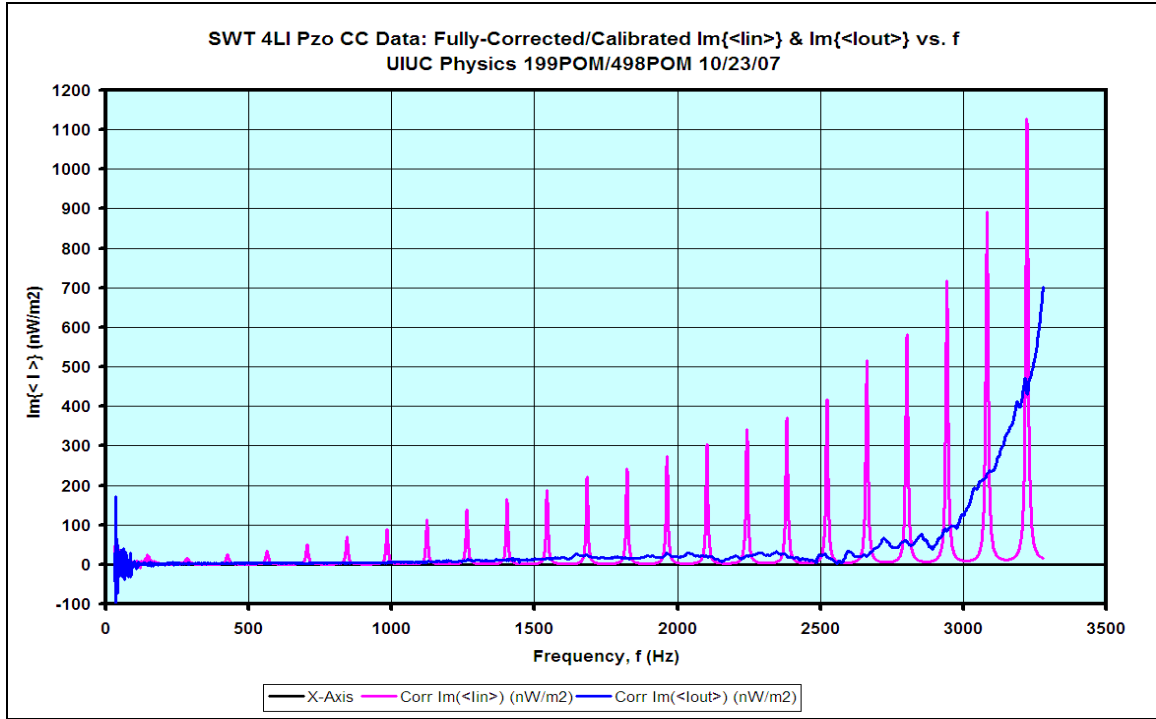A plot of Im(**I**) versus Re(**I**) is shown in Figure 63.

Figure 60. Real component of the internal (pink) and external (blue) phase corrected longitudinal intensity as a function of frequency. The internal intensity is practically zero up to ~3000 Hz as expected.

Figure 61. Imaginary component of the internal (pink) and external (blue) phase corrected longitudinal intensity as a function of frequency. The imaginary internal intensity is the only component that contributes to the magnitude of the internal longitudinal intensity.
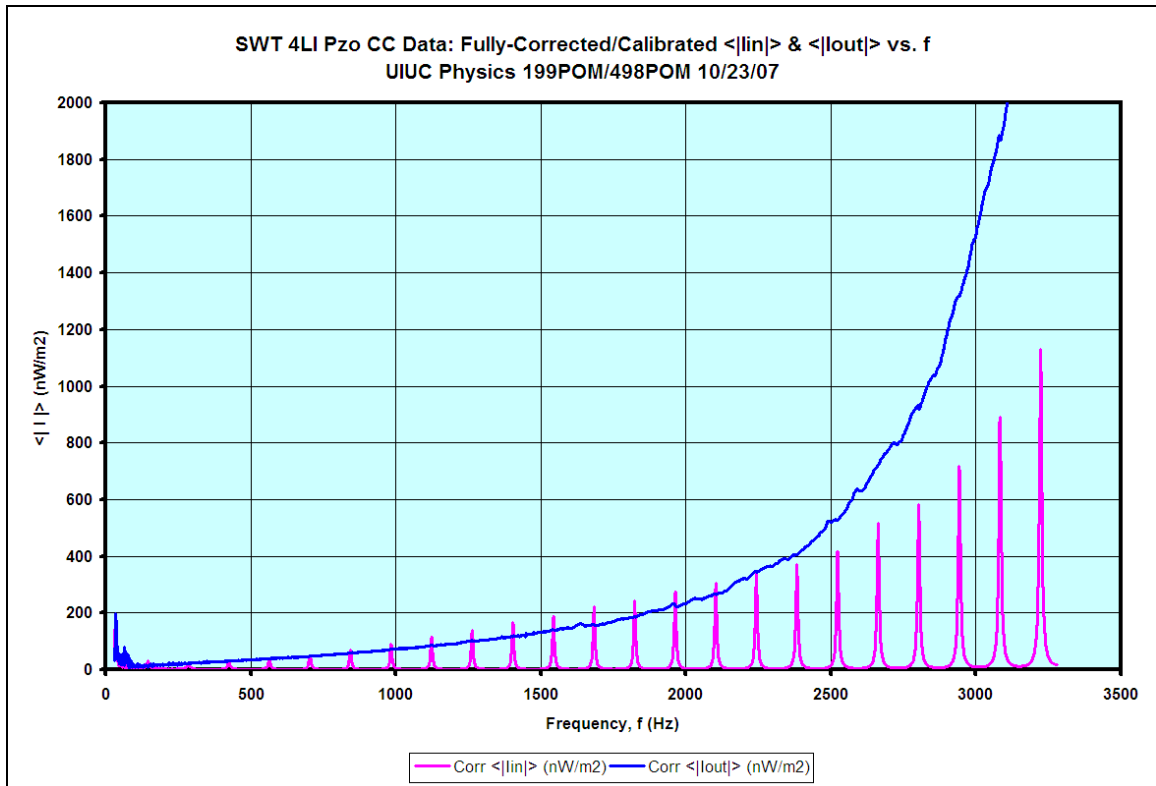
Figure 62. Magnitude of the complex longitudinal intensity as a function of frequency.
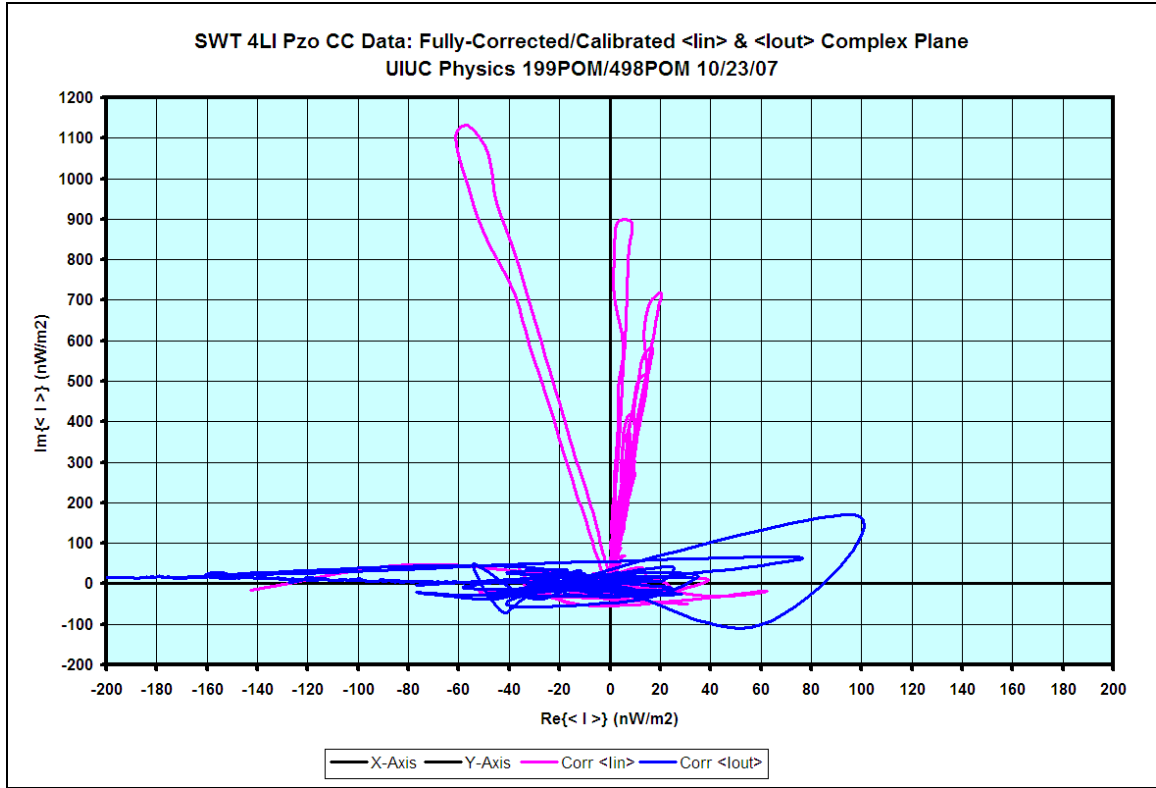
*Figure 63. Internal (pink) and external (blue) Im(**I**) versus Re(**I**) (in nW/m^2) for the SWT on the complex plane.*

A final way to confirm the validity of the performed phase corrections is to investigate the relation between the complex phase of the longitudinal intensity, φ_I, and the complex phase of the impedance, φ_z. By Equation 7 and Equation 8, $\varphi_{I=}\varphi_z$.

$$\frac{Z_i}{Z_r} = \left.\frac{\dfrac{p_i u_r - p_r u_i}{u_r^2 + u_i^2}}{\dfrac{p_r u_r + p_i u_i}{u_r^2 + u_i^2}}\right. = \frac{p_i u_r - p_r u_i}{p_r u_r + p_i u_i} = \frac{I_i}{I_r} \quad (7)$$

$$\varphi_I \equiv \arctan\left(\frac{I_i}{I_r}\right) = \arctan\left(\frac{Z_i}{Z_r}\right) \equiv \varphi_Z \quad (8)$$

Also, note that $\boxed{\varphi_I = \varphi_Z = \varphi_p - \varphi_u}$.

      Thus, if the performed phase corrections are correct the results of the phase for both the complex longitudinal intensity (Figure 64) and the complex impedance (Figure 65) should be identical. Comparing Figure 64 and Figure 65 verifies this result and the performed phase corrections.
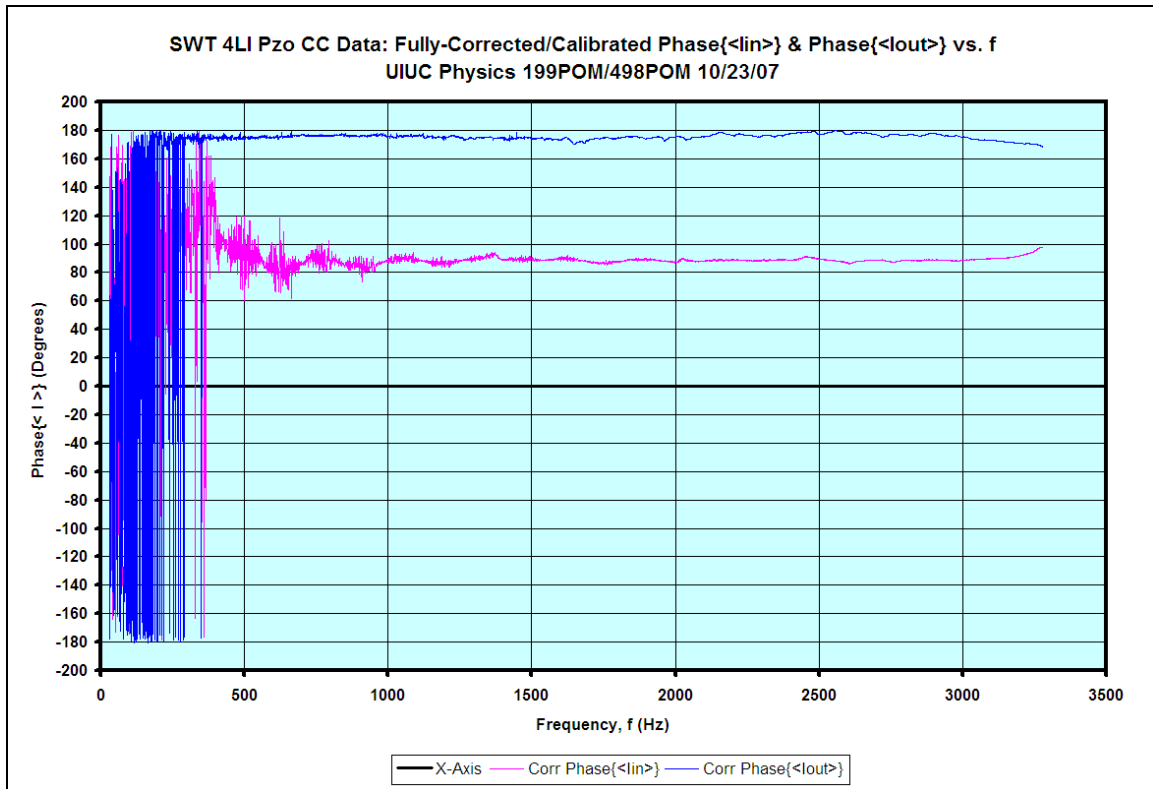

Figure 64. Corrected complex phase plot of the longitudinal internal (pink) and external (blue) intensity as a function of frequency. Note: This plot is identical to the complex phase plot of the impedance.
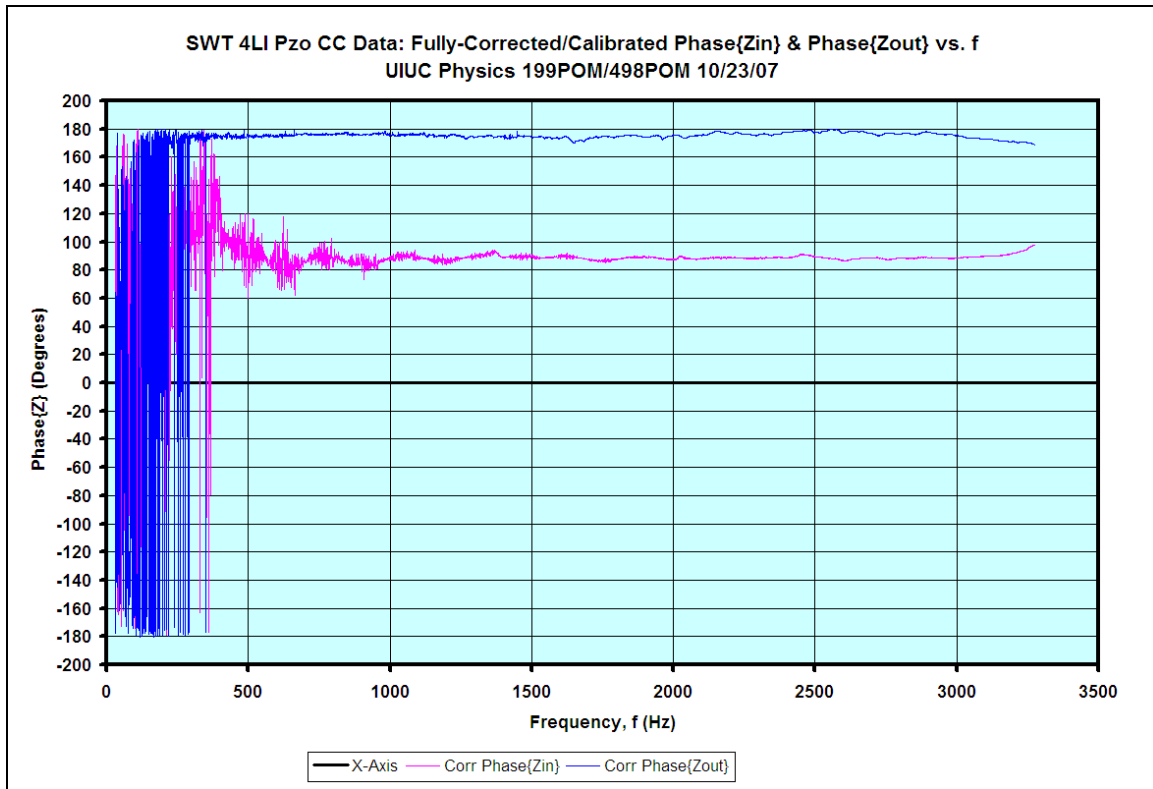
Figure 65. Corrected complex phase plot of the internal (pink) and external (blue) impedance as a function of frequency. Note: This plot is identical to the complex phase plot of the longitudinal intensity.

A plot of the sound intensity factor for the SWT is shown in Figure 66.
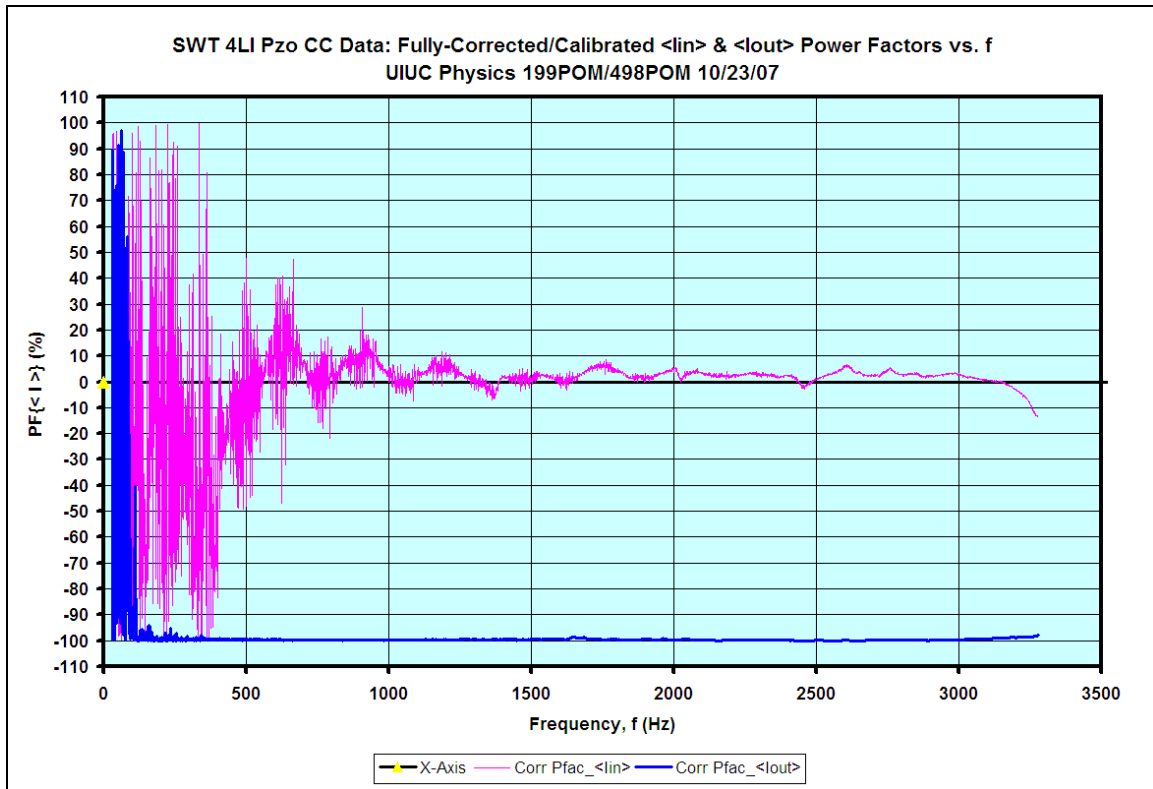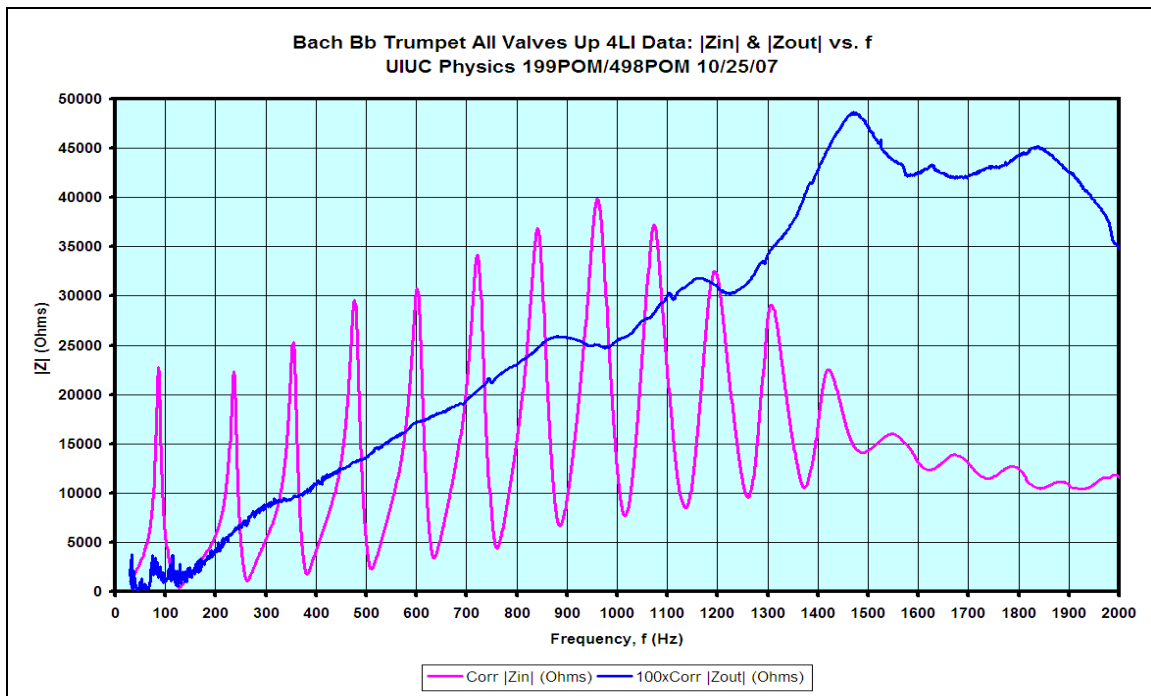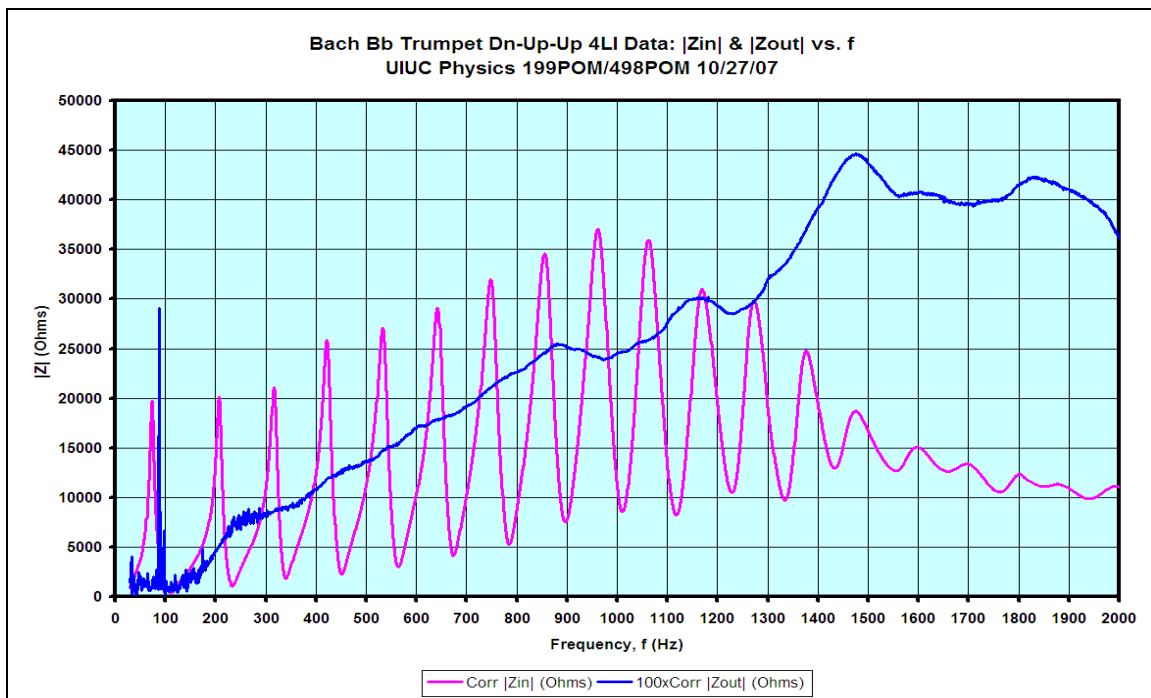
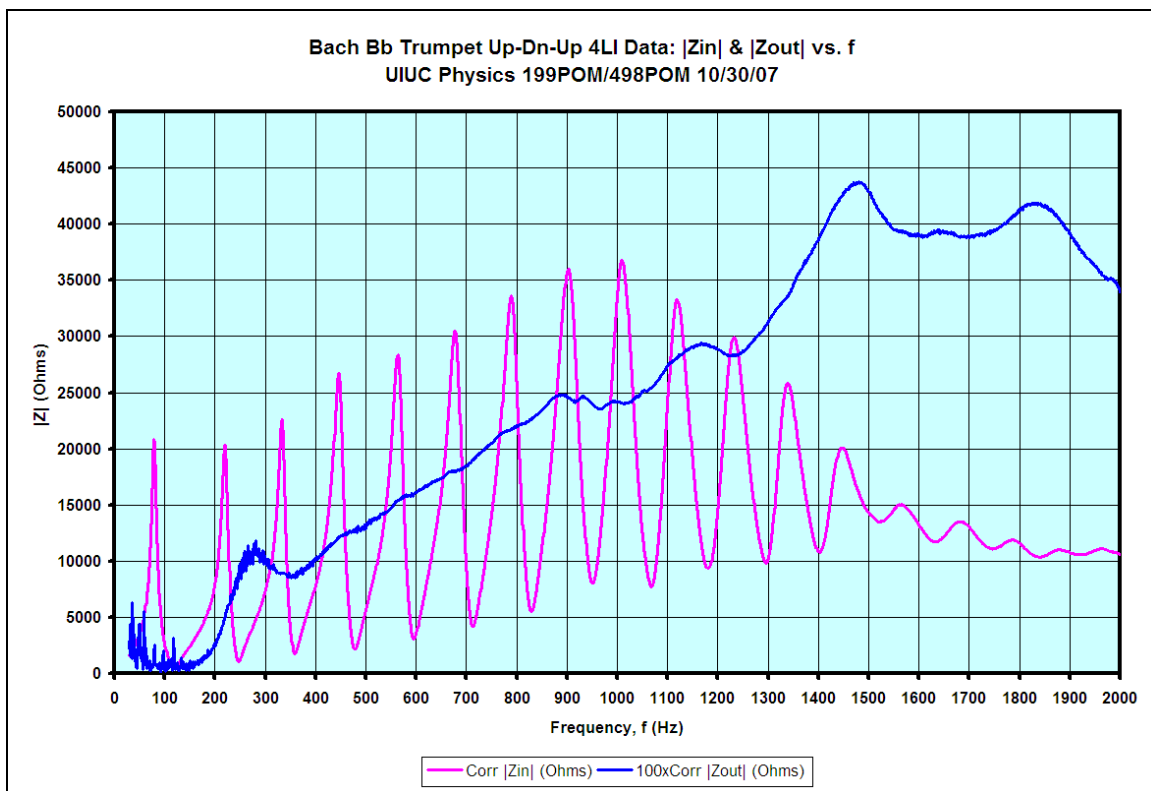*Figure 66. Internal (pink) and external (blue) sound intensity factor as a function of frequency for the SWT.*

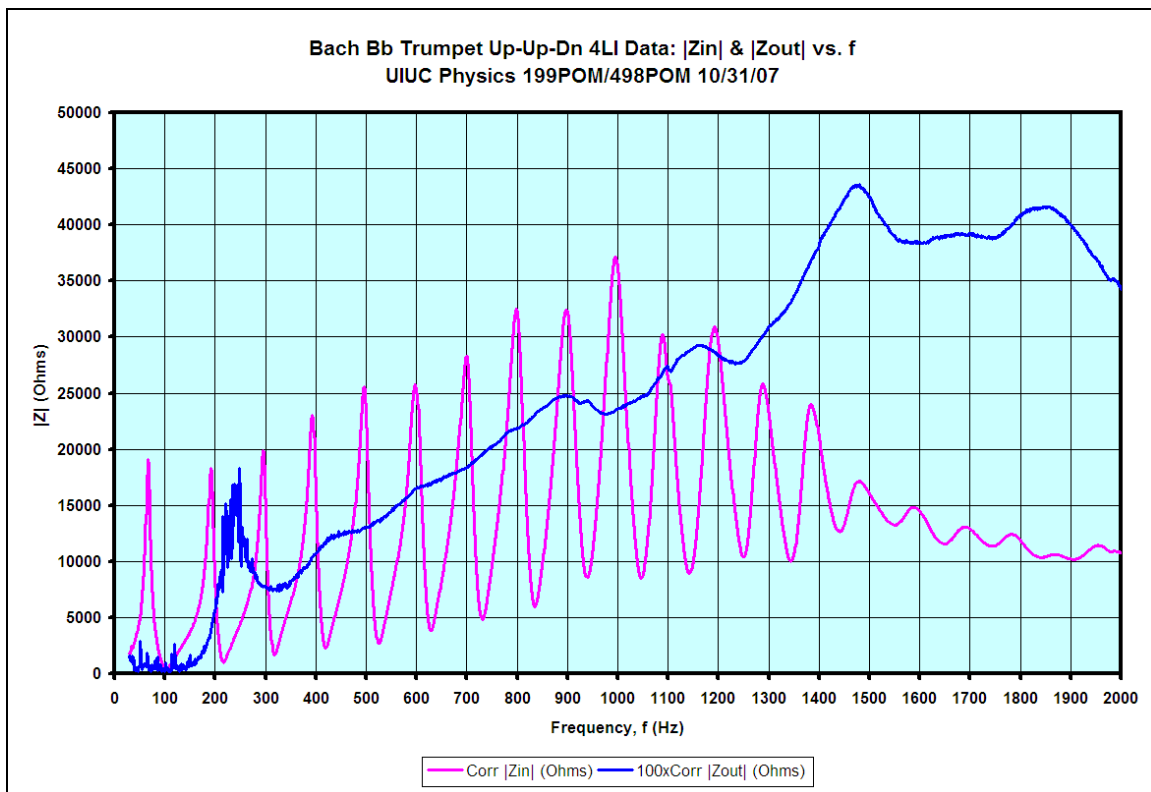# Appendix IV. Input and Output Impedance Spectra of All Valve Combinations
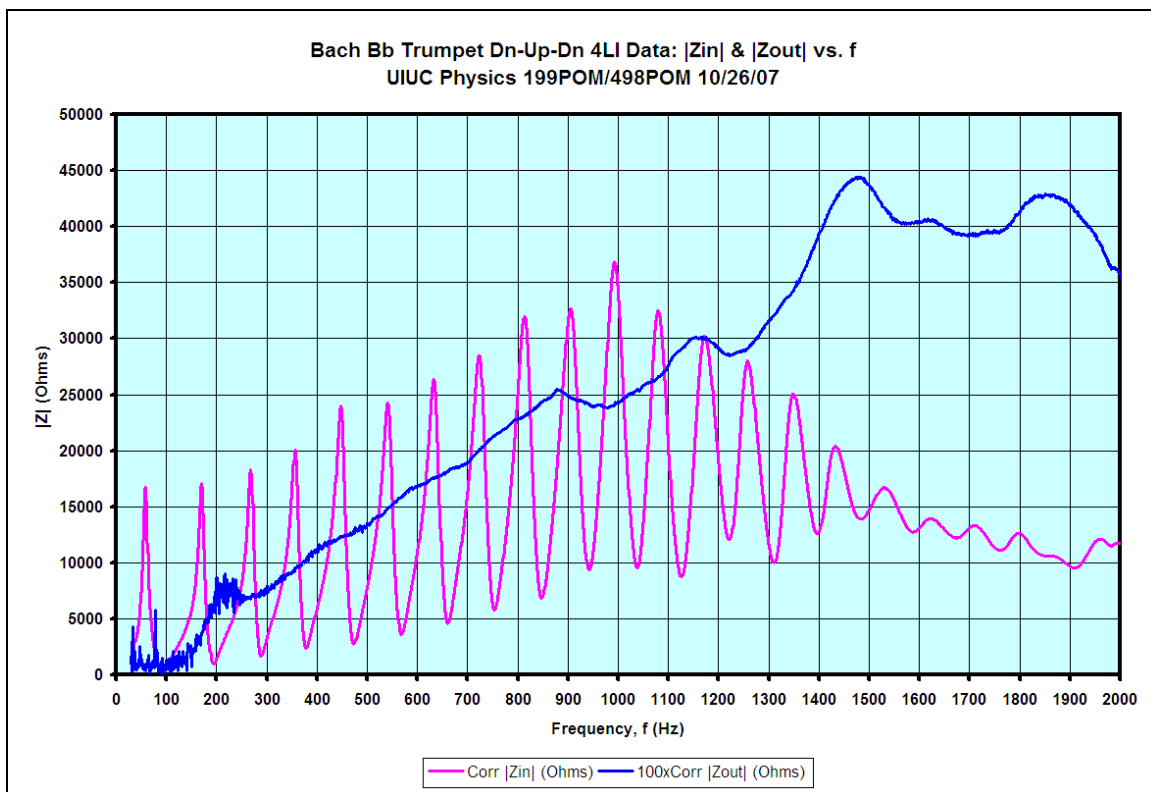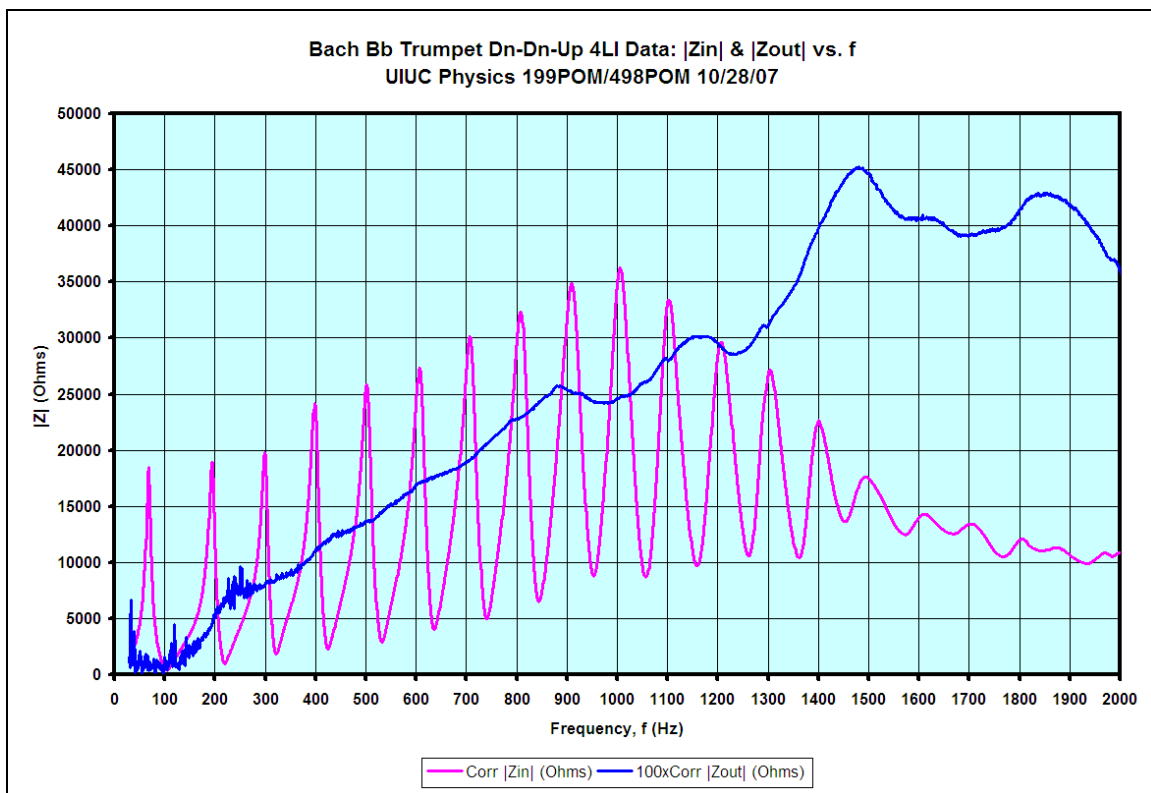

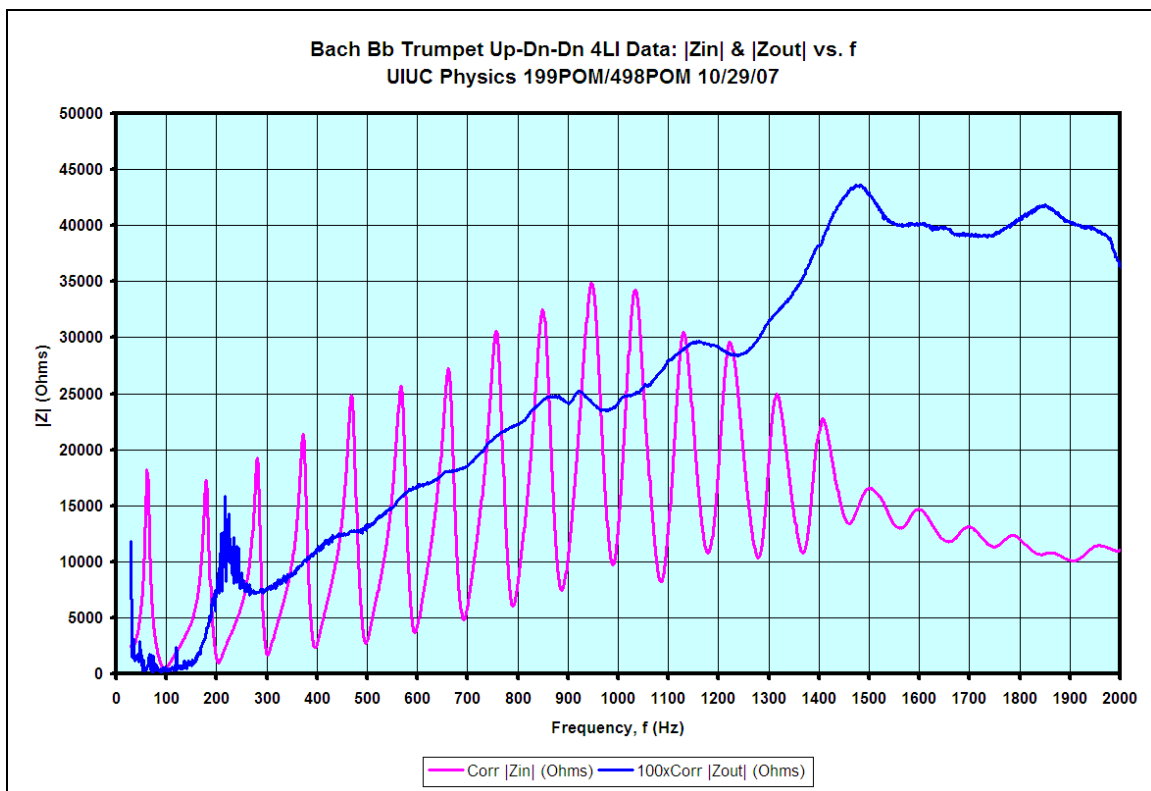*All Valves Open (OOO)*

First Valve Closed (XOO)

Second Valve Closed (OXO)

Third Valve Closed (OOX)

First Two Valves Closed (XXO)
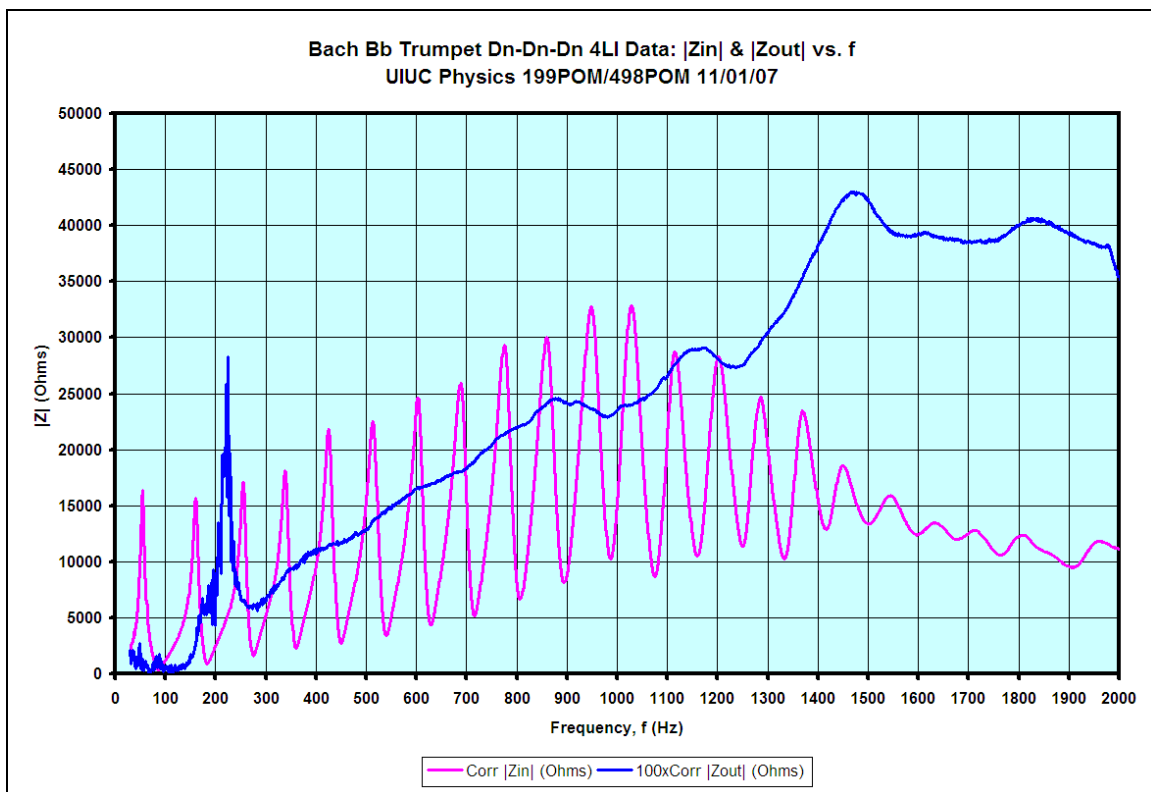

First and Third Valve Closed (XOX)

Last Two Valves Closed (OXX)

All Valves Closed (XXX)

Appendix V. Wave Analysis of a C4 (~233 Hz) Note

Using a wave analysis program developed by Joseph Yasi, a phase-sensitive wave analysis on a C4 (~233 Hz) note—played by the author himself—was carried out.[14] The results presented in this appendix are specific to the recording of the note being analyzed. A different player playing the same note—even the same player playing the note on a different day—could produce slightly different results.

The harmonic spectrum for the C4 note is shown in Figure 67. The harmonics contained in this spectrum and their relative amplitudes determine the timbre of the note being played. A 3D plot of the time-dependent harmonic spectrum is shown in Figure 68.
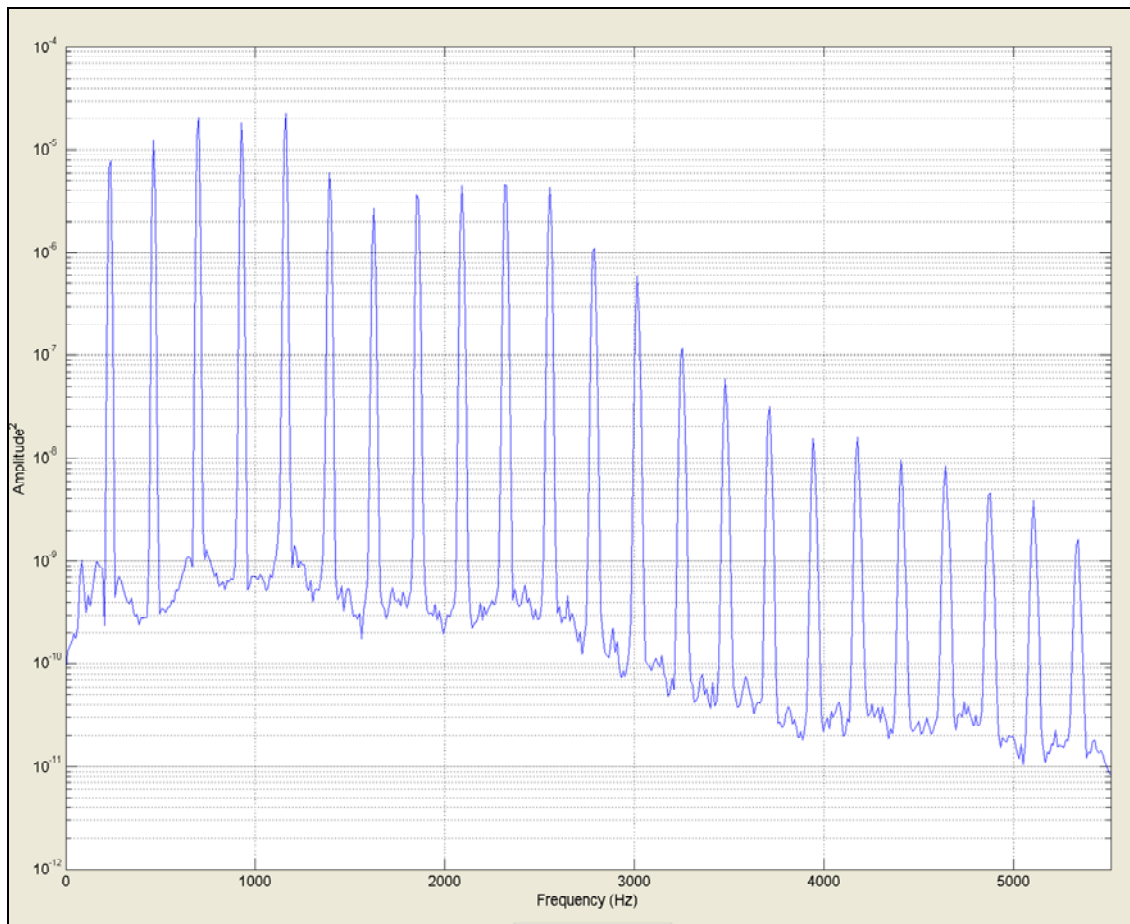

Figure 67. Harmonic spectrum of a C4 (~266 Hz) note played on a Bb trumpet.
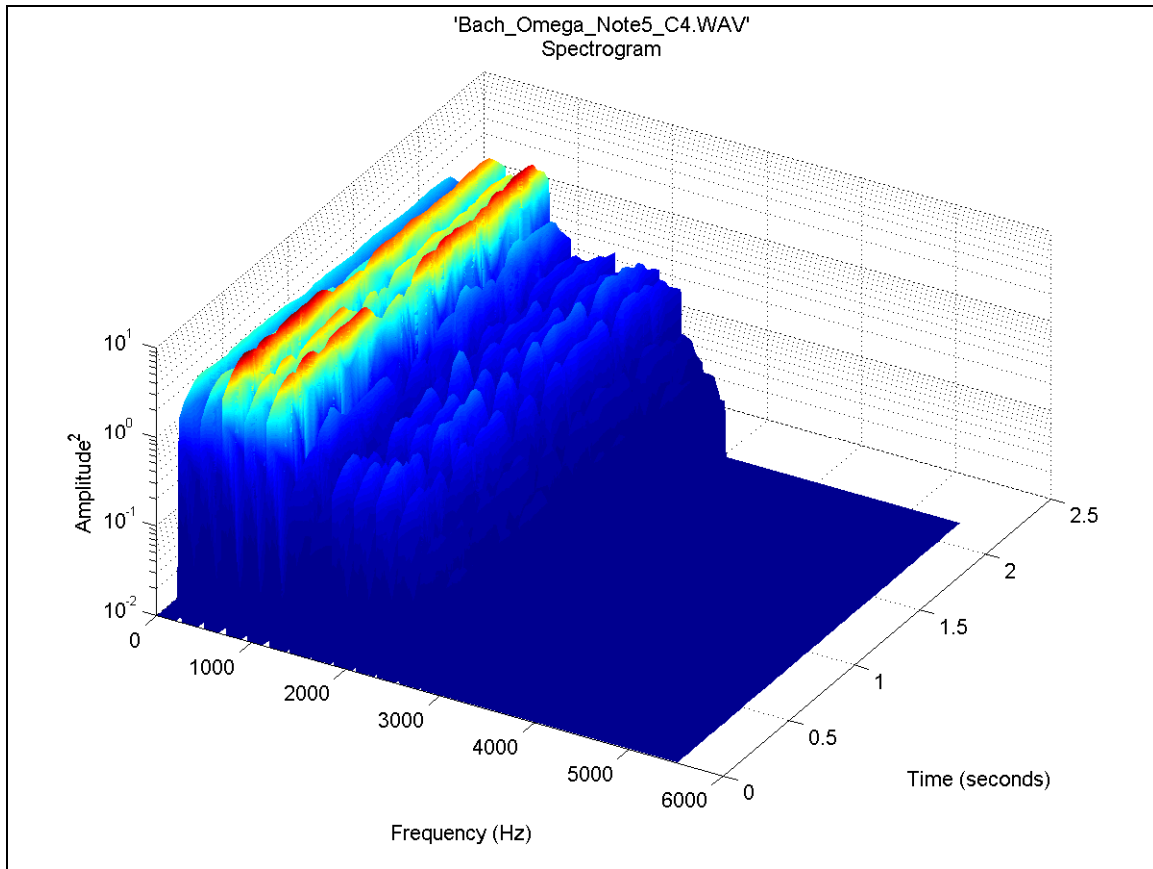
Figure 68. Three dimensional plot of the time-dependent harmonic spectrum of the C4.

A plot of the amplitudes of the first seven harmonics as a function of time is shown in Figure 69. The amplitudes of the first few harmonics are stable throughout the two second analysis period. As the harmonic number increases the amplitudes become less stable. A more experienced trumpet player should be able to keep the amplitudes of the higher harmonics as constant as the amplitudes of the lower harmonics.
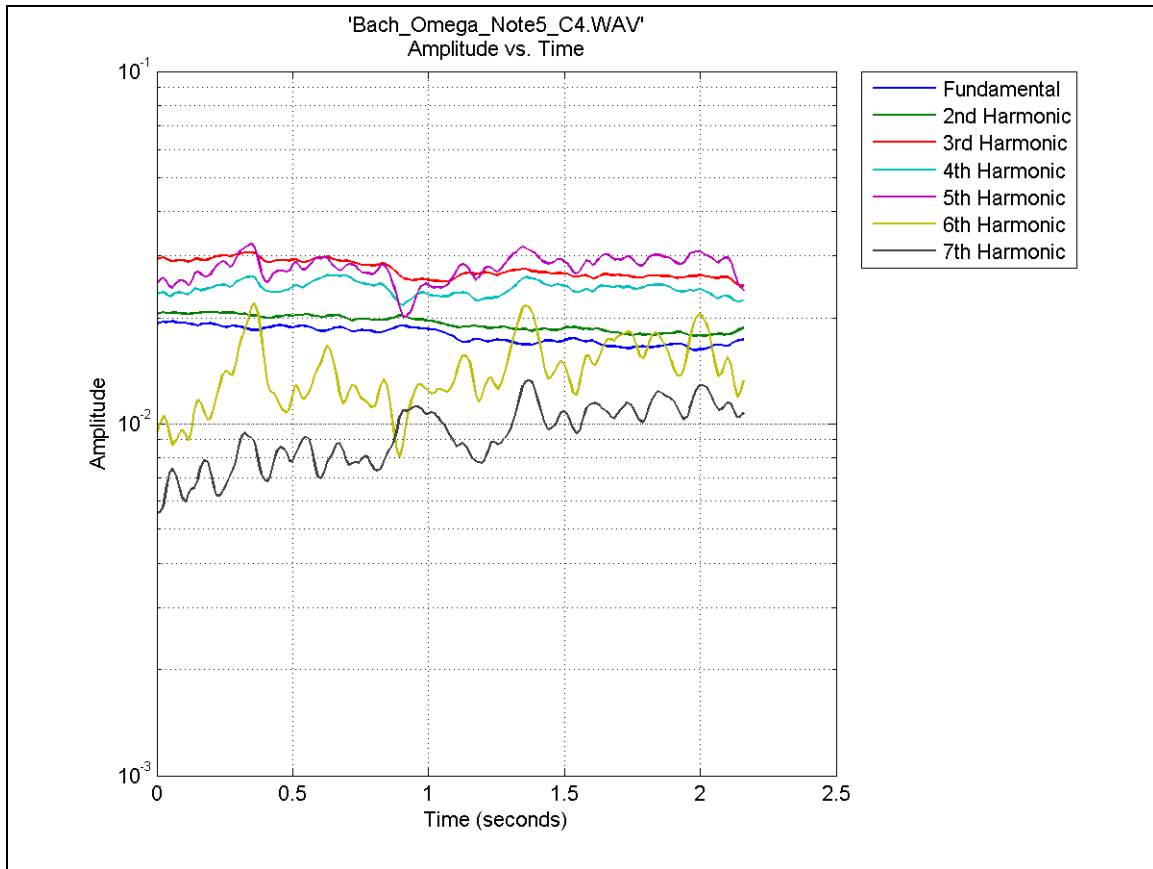
Figure 69. Amplitudes of the first seven harmonics of the C4 as a function of time.

A plot of the frequencies of the first seven harmonics as a function of time is shown in Figure 70. Although the amplitudes of the higher harmonics fluctuate more than the lower harmonics throughout the two second analysis period, the frequencies of the harmonics remain fixed as the harmonic number increases.
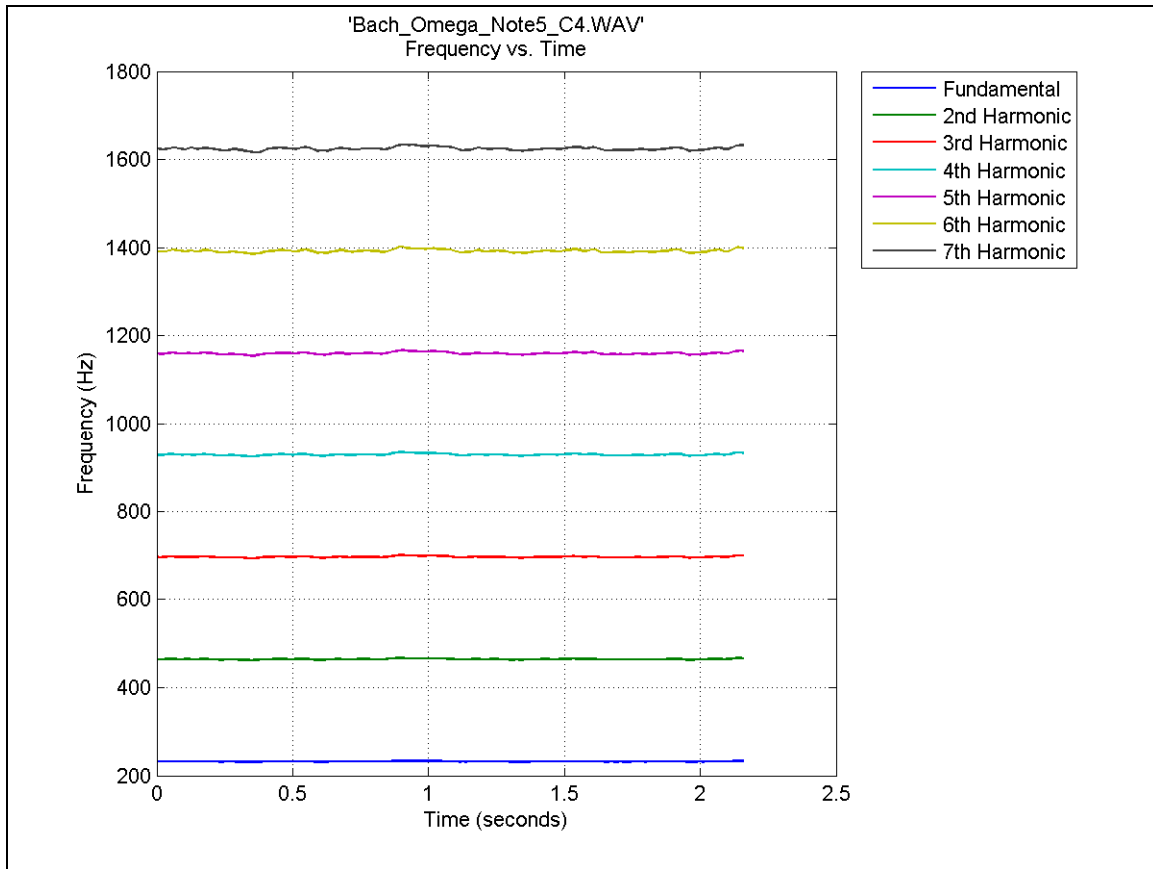
Figure 70. Frequencies of the first seven harmonics of the C4 as a function of time.

A plot of the phases of the harmonics relative to the fundamental frequency as a function of time is shown in Figure 71. As was the case with the amplitudes of the harmonics, as the harmonic number increases, the relative phase becomes less stable.
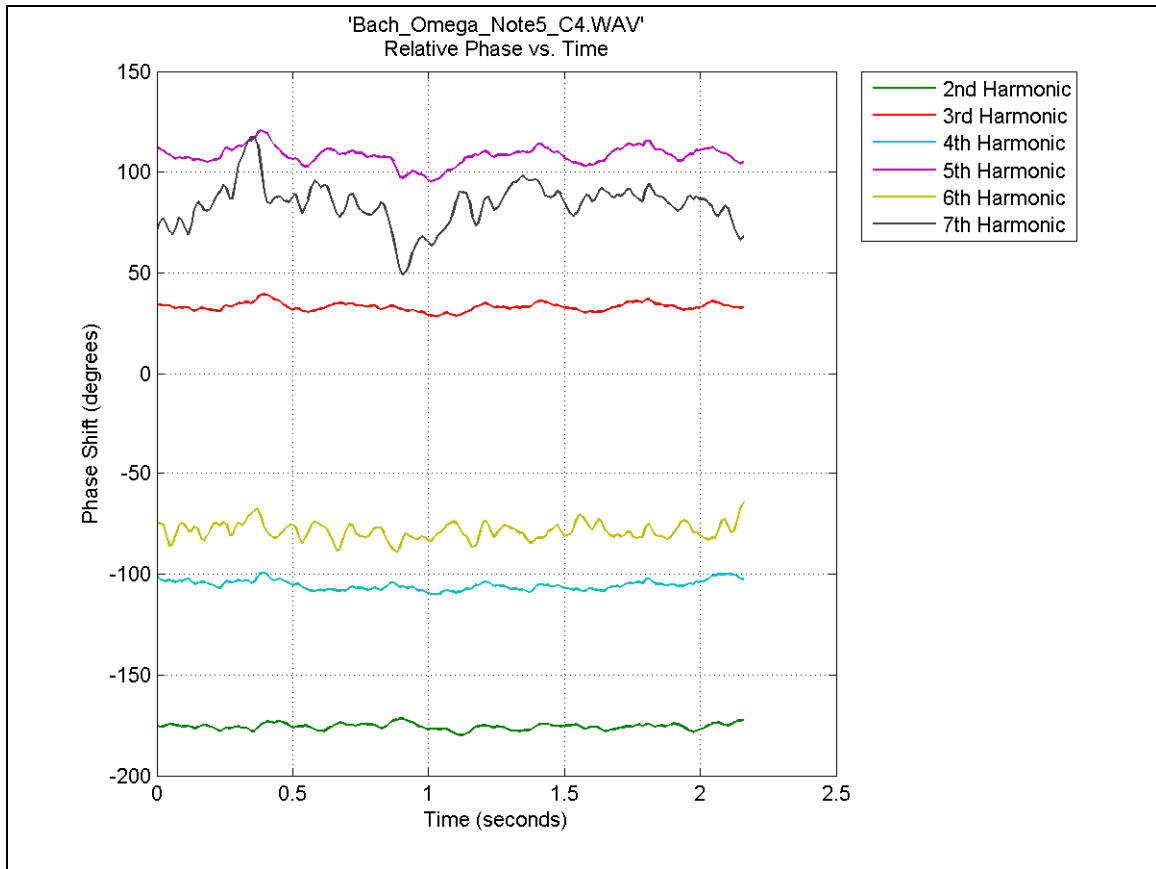
Figure 71. Phases of the harmonics relative to the fundamental frequency as a function of time.

A phasor diagram of the first seven harmonics is shown in Figure 72. A plot

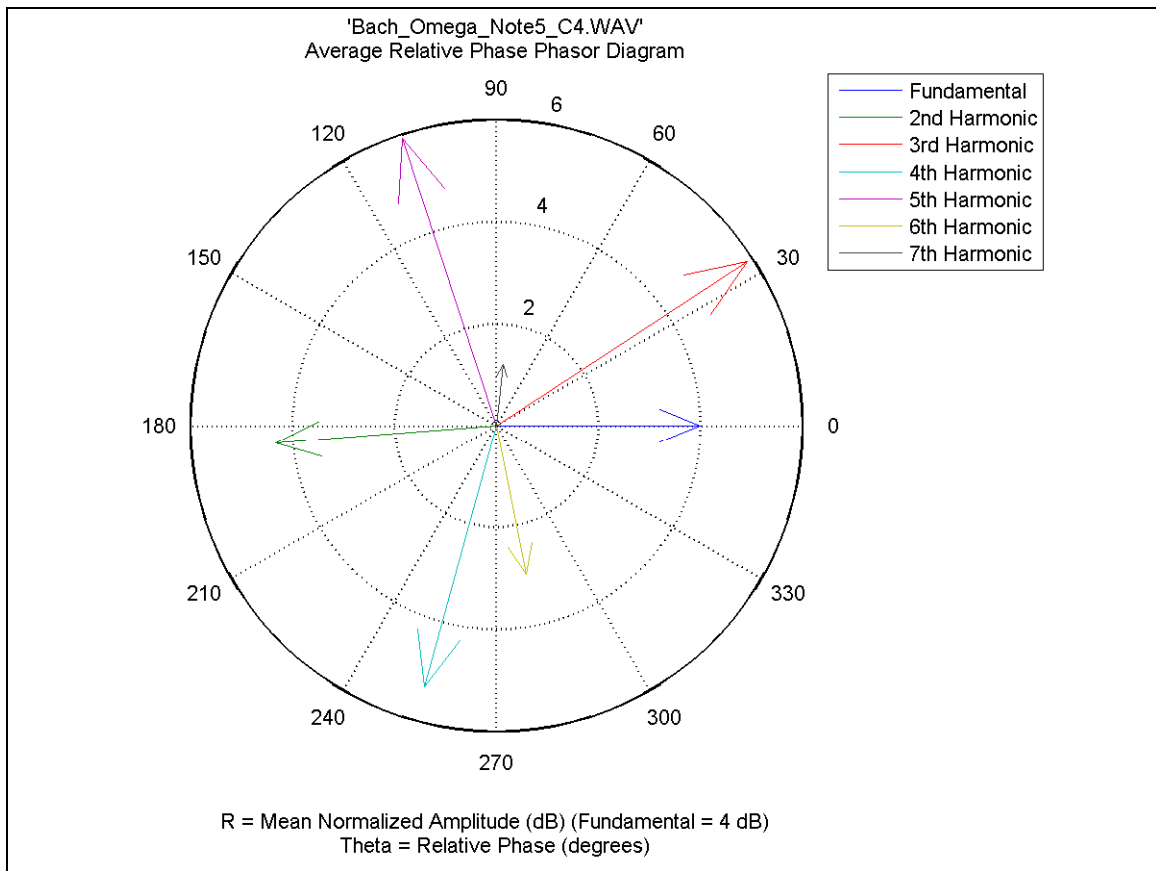showing the amplitudes of the first seven harmonics on a dB scale is shown in Figure 73.

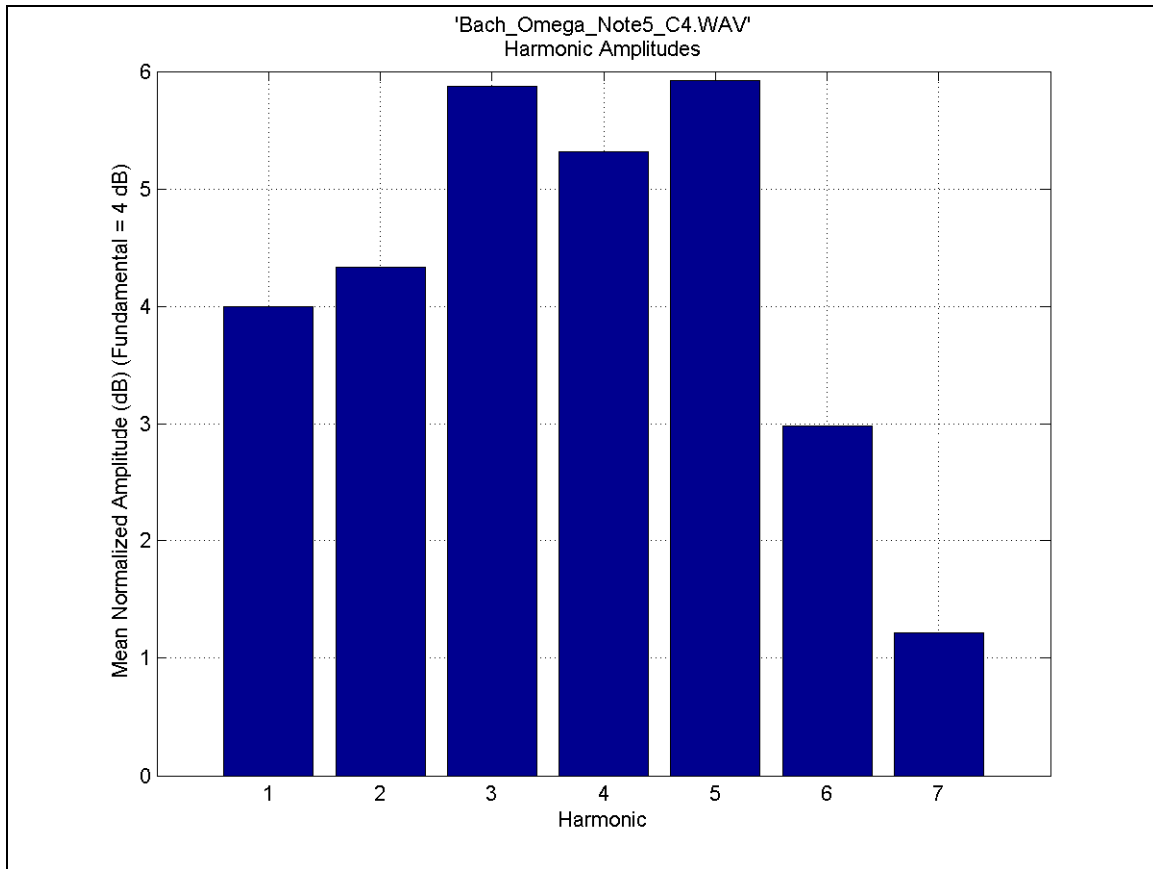*Figure 72. Phasor diagram of the first seven harmonics of the C4.*

Figure 73. Amplitudes of the first seven harmonics of the C4 on a dB scale.

References

[1]J. Backus, J. Acoust. Soc. Am. 54, 470 (1974).

[2]J. Jeans, "The Vibrations of Air," in Science &Music (Dover Publications, New York, 1968), Ch. IV, pp. 107–151.

[3]T. Moore, International Trumpet Guild Journal 27, 70 (2002).

[4]J. Backus, J. Acoust. Soc. Am. 60, 1266 (1976).

[5]A.H. Benade, J. Acoust. Soc. Am. 81, 1152 (1987).

[6]D. Pignotti and C. Van de Riet, "Input Impedance Spectrum for a Tenor Sax and a Bb Trumpet" (unpublished).

[7]H.C. Bennet-Clark, J Exp Biol. 108, 459-463 (1984)

[8]S. Errede, presented at the Audio Engineering Society, University of Illinois at Urbana-Champaign, Nov 9, 2005 (unpublished).

http://online.physics.uiuc.edu/courses/phys498pom/Lecture_Notes/Guitar_Pickup_Talk/Electronic_Transducers_for_Musical_Instruments.pdf (August 1, 2007)

[9]W. Kausel, IEEE Transactions on Instrumentation and Measurement 53, 4 (2004)

[10]Knowles Electronics, FG-23329-C05 datasheet,

http://www.knowles.com/search/prods_pdf/FG-23329-C05.pdf (January 10, 2008)

[11]Knowles Electronics, EK-23132 datasheet,

http://www.knowles.com/search/prods_pdf/EK-23132-000.pdf (January 10, 2008)

[12]RadioShack, PC-Mount condenser Microphone Element,

http://www.radioshack.com/product/index.jsp?summary=summary&techSpecs=techSpecs&currentTab=techSpecs&custRatings=custRatings&features=features&accessories=accessories&productId=2062215&support=support&tab=accessories (January 10, 2008)

[13]S. Errede, SWT Theory,

http://online.physics.uiuc.edu/courses/phys199pom/NSF_REU_Reports/SWT_Theory.pdf

[14]J. Yasi, "An Algorithm for Extracting the Relative Phase of Harmonics from a Periodic Digital Signal"

http://online.physics.uiuc.edu/courses/phys199pom/NSF_REU_Reports/2004_reu/Joe_Yasi_Final_Paper.pdf